# Measurement of Ξ ?atomic X rays using iron target

| | |
|---|---|
| 著者 | Ishikawa Yuji |
| 学位授与機関 | Tohoku University |
| URL | http://hdl.handle.net/10097/00137428 |

# Measurement of $\Xi^-$ atomic X rays using iron target

# （鉄標的を用いた$\Xi$原子X線測定の研究）

Tohoku University

Yuji Ishikawa

2022

# Abstruct

X-ray spectroscopy of $\Xi^-$ atom is a valid method to study the $\Xi^-$-nuclear interaction, since the shift of the X-ray energy from that considering only the Coulomb interaction and the width of the X-ray peak depend on the depth of the real and the imaginary parts of the $\Xi$-nucleus potential, respectively.

$\Xi^-$ Fe atomic X-ray spectroscopy experiment, J-PARC E03 was performed in 2020-2021 to observe the $\Xi^-$ atomic X ray for the first time in the world and obtain information on the $\Xi^-$-nuclear interaction. $\Xi^-$ particles were produced in an iron target by the $(K^-, K^+)$ reaction with a 1.8 GeV/$c$ $K^-$ beam. For particle identification and momentum analysis, the beam line spectrometer and the KURAMA spectrometer were used for beam $K^-$ particles and scattered $K^+$ particles, respectively. On the other hand, the germanium detector array, Hyperball-X' was used to detect the X rays from $\Xi^-$ Fe atom.

The $\Xi^-$ Fe atomic X-ray spectrum was obtained in coincidence with the $(K^-, K^+)$ reaction. In the preset study, no clear peak with $3\sigma$ significance was observed. An upper limit of the X-ray intensity per stopped $\Xi^-$ for $(7I \to 6H)$ transition of $\Xi^-$Fe atom, was estimated to be 0.19.

# Contents

# List of Figures

# List of Tables

# Chapter 1

# Introduction

## 1.1 Strangeness nuclear physics

Nucleons ($N$), namely protons and neutrons, consist of only up and down quarks. On the other hand, the baryons ($B$) which contain strange quarks in addition to up and down quarks are called hyperons ($Y$). Figure 1.1 shows the baryon octet with a spin of 1/2 represented using z component of isospin ($I_3$) and strangeness ($S$). The interaction between octet baryons in the flavor SU(3) symmetry is decomposed into the following irreducible representations,

$$8 \otimes 8 = 27 \oplus 10^{*} \oplus 10 \oplus 8_s \oplus 8_a \oplus 1. \tag{1.1}$$

The 27-plet and $10^*$-plet terms, which the $NN$ interactions belong to, are well known phenomenologically. The other multiplets appear by adding strangeness. In particular, the singlet term appears only in the $S = -2$ sector. In order to understand the origin of nuclear force ($NN$ interaction), it is necessary to investigate the whole system of the baryon-baryon (BB) interactions, and for this purpose the study of $YN$ and $YY$ interactions play essential roles.

$NN$ interaction has been studied by $NN$ scattering experiments. In contrast, experimental data of $YN$ and $YY$ scatterings are limited due to short lifetimes of hyperons, although recently, precise data of $\Sigma N$ scattering has started to be obtained [1]. Therefore, the $BB$ interaction in the $S = -1$ systems has been studied by investigating structure of hypernuclei: nuclei containing a hyperon [2]. The spectroscopy of hypernuclei has clarified that $\Lambda N$ interaction is attractive and $\Sigma N$ interaction is repulsive. The $\Sigma N$ interaction was also studied by $\Sigma^-$ atomic X-ray spectroscopy [3] [4] [5]. On the other hand, for the $BB$ interaction in the $S = -2$ sector such as $\Xi N$ interaction, experimental data are sparse.

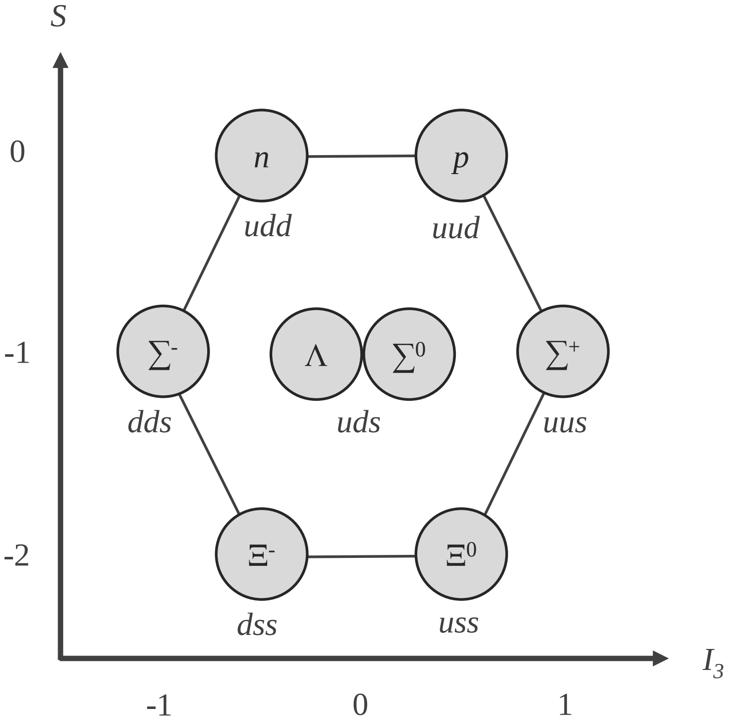

Figure 1.1: Baryon octet in the flavor SU(3) symmetry with a spin of 1/2. $I_3$ and $S$ are the z component of isospin and the strangeness, respectively.

## 1.2 $\Xi N$ interaction

The $YN$ and $YY$ interactions in the $S = -2$ sector are also important to understand the baryon-baryon interaction under the flavor SU(3) symmetry. In the $S = -2$ sector, a strong mixing between $\Xi N$ and $\Lambda\Lambda$ is expected because of their small mass difference of 28 MeV. The mass difference is much smaller than that of $S = -1$ ($\Lambda N - \Sigma N$) and 0 ($NN - \Delta N$). Since the mixing effect is inversely proportional to the mass difference, the $S = -2$ system may be the first system where the baryon mixing effect plays a dominant role. In addition, understanding of the $\Xi N$ interaction is necessary to reveal a role of $\Xi^-$ in neutron stars. In the core of a neutron star, where a high-density condition (2-3$\rho_0$) is expected, hyperons would appear because the Fermi energy of neutron becomes larger than the mass difference between a hyperon and a nucleon. Figure 1.2 shows the calculated fractions of baryons and leptons in the neutron star matter [6]. In particular, the hyperons with negative charge, $\Sigma^-$ and $\Xi^-$, can reduce large the Fermi energy of electron. However, $\Sigma^-$s would not appear in neutron stars due to the strongly repulsive $\Sigma N$ interaction. Therefore, $\Xi^-$ is a candidate of hyperons that appear in the neutron stars in an early stage when the neutorn star is compressed and the density goes up.

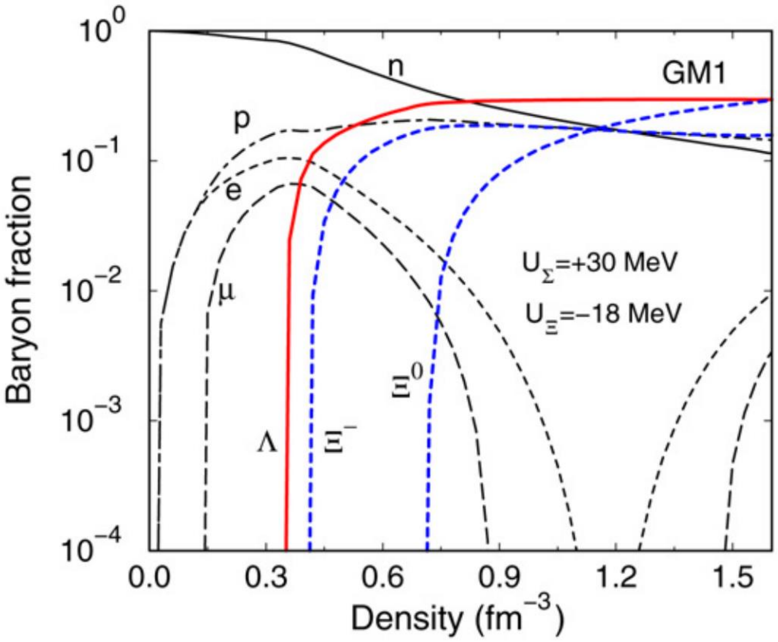

Figure 1.2: Fractions of baryons and leptons in the neutron star matter for a relativistic mean-field calculation using the parameter set GM1 [6].

Various theoretical studies on the $\Xi N$ interaction have been conducted. The Nijmegen group has constructed various baryon-baryon interaction models based on one boson exchange picture. Most of the models predict a repulsive the $\Xi N$ interaction, while a recent model called ESC16 presented an attractive $\Xi N$ interaction [7]. The HAL QCD group has started to provide $BB$ interactions with a lattice QCD method. Recently, a lattice QCD calculation near the physical point presented a $\Xi N$ potential which shows a $\Xi N - \Lambda\Lambda$ interaction much weaker than those of the Nijmegen model [8]. Chiral effective field theory is also a powerful new tool for understanding $BB$ interactions [9].

## 1.3 Experimental studies on $\Xi N$ interaction

As described in the previous section, $\Xi N$ interaction is important for various reasons. In this section, experimental studies on $\Xi N$ interaction in the past are described.

### 1.3.1 Spectroscopy of $\Xi$ hypernuclei

A missing mass spectroscopy experiment of $\Xi$ hypernucei was performed in the BNL AGS E885 experiment [11]. In this experiment, the missing mass in the $^{12}\mathrm{C}(K^-, K^+)$ reaction was measured using magnetic spectrometers. A comparison of the obtained continuum spectral shape with a theoretical calculation assuming a Woods-Saxon shape potential suggested that the $\Xi$-nucleus potential is weakly attractive with a depth of $\sim$14 MeV. Bound state peaks, that could strongly constrain the potential, were not observed.

### 1.3.2 Study of $\Xi^-$ bound system with emulsion

Nuclear emulsion has been also used to study of the $\Xi N$ interaction. In the emulsion experiments, produced $\Xi^-$ hyperons by the $(K^-, K^+)X$ reaction are absorbed by nuclei in the emulsion such as C, N and O. Some emulsion experiments reported production of a pair of single $\Lambda$ hypernuclei, namely, twin $\Lambda$ hypernuclei. These hypernuclei are produced after the formation of a $\Xi^-$ atom. The binding energy of the $\Xi^-$ hyperon, $B_{\Xi^-}$, of the $\Xi^-$ atomic/nuclear state which undergoes $\Xi^-$ absorption reaction ($\Xi^- p \rightarrow \Lambda\Lambda$) is obtained by identifying all decay fragments including the pair of single $\Lambda$ hypernuclei and measuring their kinetic energies.

Information on $\Xi$-nucleus systems can be obtained from twin $\Lambda$ hypernuclei events. In the 1990s, the emulsion experiments, KEK E176 and the KEK E373 were performed. In the KEK E176 experiments, two events of twin $\Lambda$ hypernuclei production were observed [13] [14]. Both events were interpreted as $\Xi^- + {}^{12}\mathrm{C} \rightarrow {}^{9}_{\Lambda}\mathrm{Be} + {}^{4}_{\Lambda}\mathrm{H}$, as most probable decay mode. In 2014, a twin $\Lambda$ hypernuclear event, named "KISO", was found from the data of the KEK E373 experiment [16]. The event was uniquely interpreted as $\Xi^- + {}^{14}\mathrm{N} \rightarrow {}^{10}_{\Lambda}\mathrm{Be} + {}^{5}_{\Lambda}\mathrm{He}$. The $B_{\Xi^-}$ value of the KISO event was obtained to be 3.87 ± 0.21 MeV or 1.03 ± 0.18 MeV for the ${}^{10}_{\Lambda}\mathrm{Be}$ nucleus produced as the ground state or the first excited state, respectively [17].

Furthermore, the J-PARC E07 experiment was also performed in 2016 and 2017. Table 1.1 summarizes the obtained $B_{\Xi^-}$ values of the $\Xi^- - {}^{14}\mathrm{N}$ system observed as twin hypernuclear events in the KEK E373 and the J-PARC E07 experiments.

Table 1.1: Measured $B_{\Xi^-}$ values of the $\Xi^- - {}^{14}\mathrm{N}$ system for twin hypernuclear events in the KEK E373 and the J-PARC E07 experiments.

| Experiment | Event | Daughters | $B_{\Xi^-}$ [MeV] |
|---|---|---|---|
| KEK E373 | T1 [15] | ${}^{5}_{\Lambda}\mathrm{He} + {}^{5}_{\Lambda}\mathrm{He} + {}^{4}\mathrm{He} + n$ | $-2.2 \pm 1.2$ |
| KEK E373 | T2 KISO | ${}^{10}_{\Lambda}\mathrm{Be} + {}^{5}_{\Lambda}\mathrm{He}$ | $3.87 \pm 0.21$ or $1.03 \pm 0.18$ |
| KEK E373 | T3 KINKA | ${}^{9}_{\Lambda}\mathrm{Be} + {}^{5}_{\Lambda}\mathrm{He} + n$ | $8.00 \pm 0.77$ or $4.96 \pm 0.77$ |
| J-PARC E07 | T006 IBUKI | ${}^{10}_{\Lambda}\mathrm{Be} + {}^{5}_{\Lambda}\mathrm{He}$ | $1.27 \pm 0.21$ |
| J-PARC E07 | T007 | ${}^{9}_{\Lambda}\mathrm{Be} + {}^{5}_{\Lambda}\mathrm{He} + n$ | $-1.04 \pm 0.85$ |
| J-PARC E07 | T010 IRRAWADDY | ${}^{5}_{\Lambda}\mathrm{He} + {}^{5}_{\Lambda}\mathrm{He} + {}^{4}\mathrm{He} + n$ | $6.27 \pm 0.27$ |
| J-PARC E07 | T011 | ${}^{5}_{\Lambda}\mathrm{He} + {}^{5}_{\Lambda}\mathrm{He} + {}^{4}\mathrm{He} + n$ | $0.90 \pm 0.62$ |

In the J-PARC E07 experiment, a twin $\Lambda$ hypernuclear event named "IBUKI" was observed [18]. The event was uniquely identified as $\Xi^- + {}^{14}\mathrm{N} \rightarrow {}^{10}_{\Lambda}\mathrm{Be} + {}^{5}_{\Lambda}\mathrm{He}$ with $B_{\Xi^-}$ of 1.27

± 0.21 MeV. For both KISO and IBUKI events, the energy level at which a $\Xi^-$ is absorbed is likely a Coulomb-assisted nuclear $1p$ state by considering the previous experimental suggestion ($\Xi$ potential depth of ~14 MeV) [5] and a lattice QCD calculation [8]. The $\Xi^-$ absorption in the $p$ state suggested weaker $\Xi N - \Lambda\Lambda$ coupling than that in the Nijmegen models predicting the absorption in the $d$ state.

In addition, a deeper bound state of ${}^{15}_{\Xi}\mathrm{C}$ assigned as a nuclear $s$-state was observed from two twin $\Lambda$ hypernuclear events [19]. The "KINKA" event was identified as $\Xi^- + {}^{14}\mathrm{N} \to {}^{10}_{\Lambda}\mathrm{Be} + {}^{5}_{\Lambda}\mathrm{He} + n$ with $B_{\Xi^-}$ of 8.00 ± 0.77 MeV or 4.96 ± 0.77 MeV for the ${}^{9}_{\Lambda}\mathrm{Be}$ nucleus as the ground state or the first excited state, respectively. The "IRRAWADDY" event was identified as $\Xi^- + {}^{14}\mathrm{N} \to {}^{5}_{\Lambda}\mathrm{He} + {}^{5}_{\Lambda}\mathrm{He} + {}^{4}\mathrm{He} + n$ with $B_{\Xi^-}$ of 6.27 ± 0.27 MeV. These $B_{\Xi^-}$ values are significantly larger than that for the nuclear $1p$ state. Therefore, these events are attributed to the $1s$ state of ${}^{15}_{\Xi}\mathrm{C}$. The observation of the $1s$ state of $\Xi$ hypernucleus may indicate extremely weak absorption. However, there is a claim for interpretation of the IRRAWADDY event [20].

### 1.3.3 Study of $p\Xi^-$ interaction using two-particle correlation

Recently, two-particle $p\Xi^-$ correlation was measured in $p$-Pb collision at $\sqrt{S_{NN}} = 5.02$ TeV at the LHC by ALICE collaboration [21]. The data suggested that $p\Xi^-$ interaction is more attractive than the Coulomb interaction. The lattice QCD potential provided by HAL-QCD Collaboration agreed with the measured result. This new method can provide information on a low energy part of the $p\Xi^-$ interaction.

### 1.3.4 Measurement of $\Xi^-$ atomic X ray

The first experiment for measurement of $\Xi^-$ atomic X ray, J-PARC E07 experiment, was performed at the J-PARC K1.8 beam line in 2016 and 2017. In this experiment, the X rays from $\Xi^-$C, $\Xi^-$Ag and $\Xi^-$Br atoms were tried to be measured. In this subsection, X-ray spectroscopy of exotic atoms and the measurement of $\Xi^-$ atomic X-ray spectroscopy in the J-PARC E07 experiment are described.

#### X-ray spectroscopy of exotic atoms

When a negatively charged particle other than electron ($X^-$) is captured by an ordinary atom, an electron in the atom is kicked away and the exotic atom ($X^-$ atom) is formed. The captured $X^-$ transits to lower atomic orbits with X-ray emission, and is eventually absorbed by the nucleus. In the case that the $X^-$ particle is a hadron, the strong interaction works between the $X^-$ particle and the nucleus, leading to an energy shift of atomic levels. Thus, information on the $X^-$-nucleus interaction can be obtained by measuring the X rays from the $X^-$ atom. This approach has been applied successfully for various hadronic atoms such as $\pi^-$, $K^-$, $\bar{p}$ and $\Sigma^-$ atoms.

Figure 1.3 shows cascade process of the exotic atoms, de-excitation process until nuclear absorption. An $X^-$ particle captured by an atom is populated at an initial principle quantum state $n_0 \sim \sqrt{m_X/m_e}$, where $m_X$ and $m_e$ are masses of $X^-$ and electron, respectively. The population of the angular momentum $l$ state at $n_0$ is essentially statistical as follows,

$$P \sim (2l+1)\exp(\alpha l), \tag{1.2}$$

with the $\alpha$ parameter around zero. For $\mu^-$, $\pi^-$, $K^-$ atoms, reasonable results have been found for values of $\alpha$ between -0.1 and 0.1. The de-excitation occurs through Auger transition or radiative (mainly E1) transitions to a state where nuclear absorption takes place. For large principal quantum number $n$, the Auger transition with emission of the mainly K-shell electron is dominant. For lower $n$ states, radiative transition can take place. The selection rule for Auger transition is $\Delta l = \pm 1$ and preferred small $\Delta n$. On the other hand, the selection rule for radiative transition is $\Delta l = \pm 1$ and preferred large $\Delta n$. Thus, when a $X^-$ particle reached a small $n$ state, E1 transitions between circular orbits, $(n, l = n-1) \rightarrow (n-1, l = n-2)$ become the most preferred de-excitation process.

At deeper orbits, energy levels of the $X^-$ atom is shifted and broadened due to strong interaction compared with those calculated with Coulomb interaction only. The strong interaction between the $X^-$ particle and the nucleus is represented as an optical potential. The energy shift and the energy width are related with the real part and the imaginary part of the optical potential, respectively. The imaginary part of the optical potential represents the strength of nuclear absorption. In the orbits with strong absorption effects, the E1 transition to lower orbits with X-ray emission and the nuclear absorption compete with each other.

In such orbits, the X-ray yield per $X^-$ atom formation for the E1 transition $(n, l \rightarrow n-1, l-1)$ is given as

$$R_X^{(n,l\ \rightarrow\ n-1,l-1)} = BR_{E1}^{(n,l\ \rightarrow\ n-1,l-1)} \times P_{X^-(n,l)}, \tag{1.3}$$

$$BR_{E1}^{(n,l\ \rightarrow\ n-1,l-1)} = \frac{\Gamma_{E1}}{\Gamma_{E1} + \Gamma_{abs.}}, \tag{1.4}$$

where $BR_{E1}$ is a branching ratio of the E1 transition, $P_{X^-}$ is the ratio of the population of the $(n, l)$ state to the yield of $X^-$ atom. $BR_{E1}$ is represented by the widths caused by the E1 transition ($\Gamma_{E1}$) and the absorption ($\Gamma_{abs}$). When the E1 transition is dominant ($\Gamma_{E1} \gg \Gamma_{abs.}$), $BR_{E1}$ is $\sim 1$.

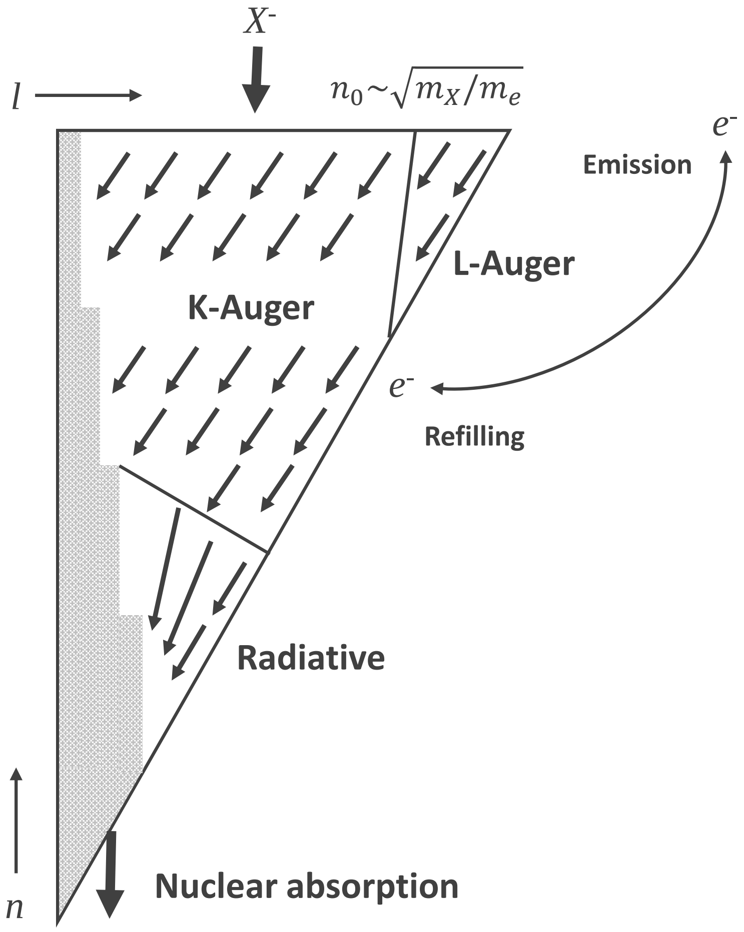

Figure 1.3: Cascade process of exotic atoms.

### $\Xi^-$ atomic X ray spectroscopy in the J-PARC E07 experiment

The J-PARC E07 experiment was performed to search for $S = -2$ hypernuclei with nuclear emulsion as described in Sec. 1.3.2. In addition to the $S = -2$ hypernuclear search, measurement of X rays from $\Xi^-$ C, Br and Ag atoms was performed in the J-PARC E07 experiment. In this experiment, quasi-free $\Xi^-$ hyperons were produced via the $p(K^-, K^+)\Xi^-$ reaction with a diamond target and were stopped in the emulsion located at downstream of the target. When a $\Xi^-$ hyperon stopped in the emulsion, it was captured by C, O, N, Br or Ag atoms contained in the emulsion and a $\Xi^-$ atom was formed. Considering atomic abundance ratio and Z dependence of the atomic capture ratio, X-ray peaks of $\Xi^-$ Br and Ag atoms were expected to be observable. Moreover, some $\Xi^-$ hyperons were also stopped in the diamond target with a 3.2 g/cm$^2$ thickness and $\Xi^-$C atom can be formed.

For tagging the $\Xi^-$ production, the missing mass of the $p(K^-, K^+)X$ reaction was reconstructed using beam $K^-$ and scattered $K^+$ momenta. The momenta of beam $K^-$s and scattered $K^+$s were measured by two magnetic spectrometers, beam line spectrometer and KURAMA spectrometer, respectively. $\Xi^-$ tracks were also measured by silicon strip detectors at upstream and downstream of the emulsion. In addition, a Ge detector array, Hyperball-X was installed near the emulsion and the diamond target for detection of the X rays from $\Xi^-$ atoms.

For $\Xi^-$ Br and Ag atoms, the expected last E1 transitions are $(7I \to 6H)$ transition (315 keV) for Br and $(8J \to 7I)$ transition (350 keV) for Ag, respectively. The emulsion analysis is ongoing and 20% of the expected number of $\Xi^-$ stop events were identified. Although the background level is low, the expected X-ray yield is a few counts with the 20% statistics and it is difficult to observe peak structure. Once emulsion analysis is completed, X-ray peaks may be observed with full statistics if the peak width is not widely broadened [22].

On the other hand, for the $\Xi^-$ C atom, the expected last E1 transition is $(3D \to 2P)$ transition (154 keV). Figure 1.4 shows a preliminary result of the $\Xi^-$C atomic X-ray spectrum and no clear X-ray peak was observed from this spectrum [23]. Figure 1.5 shows the estimated upper limit of the branching ratio of the $(3D \to 2P)$ transition for several energy regions divided based on energy shift, $\Delta E$. The upper limit assuming 1 keV peak width for 100 keV $< \Delta E \leq$ 200 keV corresponds to an X-ray yield of $(3D \to 2P)$ transition per $\Xi^-$ stop of $\sim$40%. This limit is close to a value suggested by theoretical calculation with a lattice QCD potential [24].

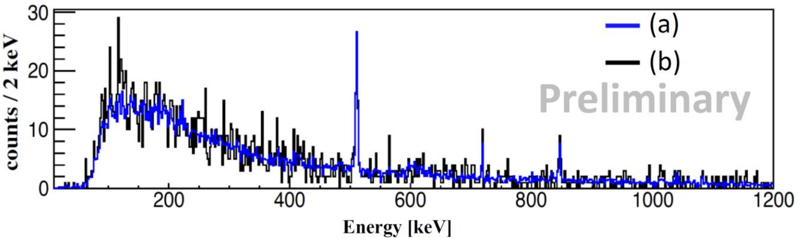

Figure 1.4: Preliminary result of the $\Xi^-$C atomic X-ray spectrum obtained in the J-PARC E07 experiment. The spectrum (a) for the events in coincidence with $\Xi^-$ prodcuntion is scaled. The spectrum (b) fro the events in coincidence with $\Xi^-$ having a large stopping probability in the target.

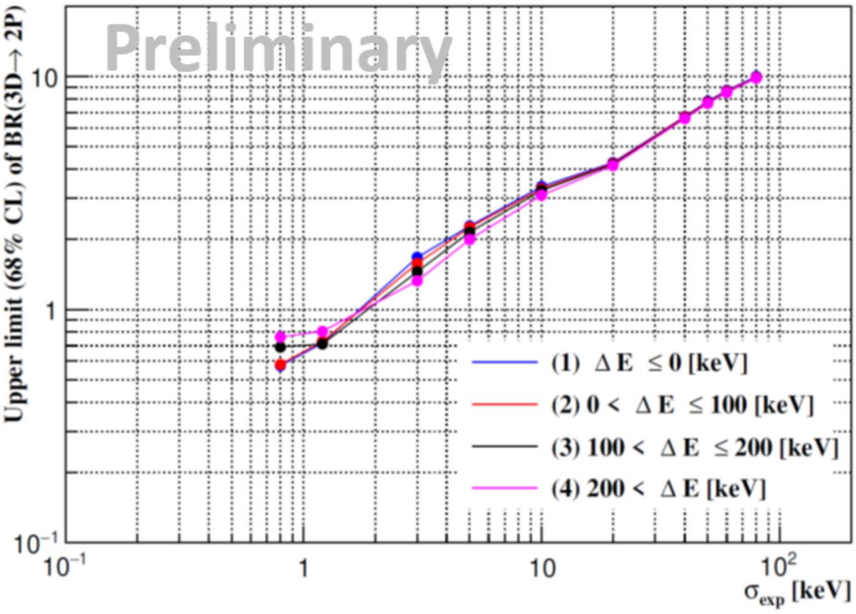

Figure 1.5: The upper limit of the branching ratio of the $(3D \to 2P)$ transition of $\Xi^-$C atom obtained in J-PARC E07 experiment. $\sigma_{exp}$ is the experimental X-ray peak width.

## 1.4 Purpose of the present research

An X-ray spectroscopy experiment of $\Xi^-$ Fe atom (J-PARC E03 experiment) was performed at the J-PARC K1.8 beam line. The purpose of this experiment was the world-first measurement of $\Xi^-$ atomic X rays to obtain information on $\Xi^-$-nucleus potential.

In this experiment, $\Xi^-$ hyperons were produced via the $p(K^-, K^+)\Xi^-$ reaction in quasi-free process on an iron target using $K^-$ beam at 1.8 GeV/$c$ where the cross section is maximum [25]. Some of produced $\Xi^-$ hyperons were slowed down and stopped in the target. The stopped $\Xi^-$ hyperon was captured by a Fe atom and a $\Xi^-$ atom are formed. The captured $\Xi^-$ hyperon transits to lower atomic orbits with X-ray emission, and the $\Xi^-$ hyperon is eventually absorbed by the nucleus. For tagging the $\Xi^-$ production, the missing mass of the $p(K^-, K^+)X$ reactions was reconstructed using beam $K^-$ and scattered $K^+$ momenta. Two magnetic spectrometer, beam line spectrometer and KURAMA spectrometer were used for the momentum analysis of the beam $K^-$s and the scattered $K^+$s, respectively. In addition, a Ge detector array, Hyperball-X', installed surrounding the target, was used for detection of the X rays from $\Xi^-$ Fe atoms in coincidence with the $(K^-, K^+)$ reaction. Details of the experimental method are described in Chapter 2.

There are reasons for using the iron target from viewpoint of experimental feasibility and physics, respectively. For the viewpoint of experimental feasibility, the following three are important points:

1. Production rate of $\Xi^-$ hyperon. The target mass dependence of the forward angle cross section of the $(K^-, K^+)$ reaction is known to be represented by $A^{0.38}$ [10]. Then, the production rate is proportional to $A^{-0.62}$ for the same target thickness.
2. Stopping probability of produced $\Xi^-$ hyperon. The target material must be dense enough to stop a reasonable fraction of the $\Xi^-$ hyperons before they decay.
3. X-ray absorption in the target.

Hence, lighter elements are better in terms of points 1 and 3, while heavier elements are better in terms of point 2. Considering these points, material with a modest X-ray absorption probability and a $\Xi^-$ production rate but a high density ($\rho > 7$ g/cm$^3$) is optimal for the X-ray yield. On the other hand, the absorption strength is important for the viewpoint of physics. The expected absorption strength at the 5G orbit of $\Xi^-$ Fe atoms corresponding to the energy width of 4 keV is suitable for our experimental method. For these reasons, iron was selected as a target in the E03 experiment.

Figure 1.6 shows the level scheme of $\Xi^-$ Fe atom. The 5G orbit is expected to be the last orbit. The energy shift (4.4 keV) and the energy width (3.9 keV) of the 5G orbit are predicted from a theoretical calculation assuming with a Woods-Saxon shape optical potential of $-24 - 3i$ MeV. On the other hand, a recent lattice QCD calculation predicts an imaginary depth more than one order of magnitude smaller. Since the J-PARC beam intensity is currently not enough to take the requested full statistics data, 10% of the full statistics data was taken as the 1st phase run. Even with 10% of the full statistics data, the X ray of the (6H $\rightarrow$ 5G) transition ($\sim$286 keV) can be observed if the peak width is less than 1 keV, which was suggested by the lattice QCD calculation. In addition, the X ray of the (7I $\rightarrow$ 6H) transition (172 keV) can be also observed without energy shift and peak broadening. Furthermore, even if the absorption strength is too weak and the information on the potential cannot be obatined from the peak structure, the yield ratio of these X rays can provide the information on the imaginary part.

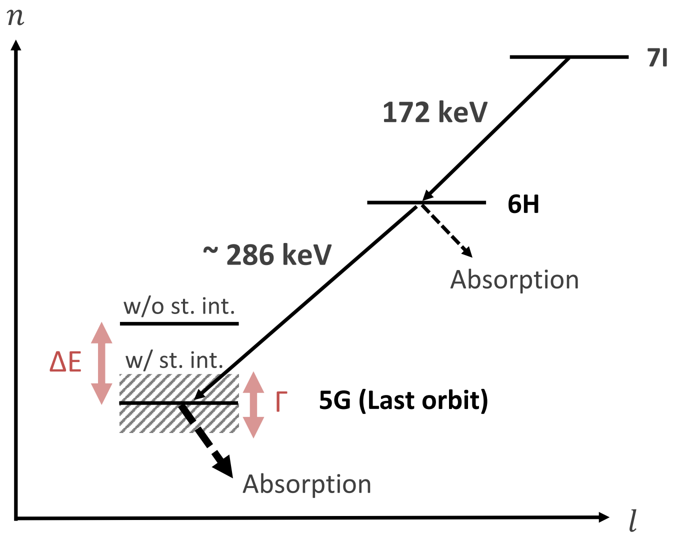

Figure 1.6: Level scheme of $\Xi^-$ Fe atom.

# Chapter 2

# Experiment

## 2.1 Overview

The $\Xi^-$-Fe atomic X-ray spectroscopy experiment (J-PARC E03) was performed at the K1.8 beam line in the J-PARC hadron experimental facility (HD) in 2020-2021. The $\Xi^-$ hyperons were produced via the quasi-free $p(K^-, K^+)\Xi^-$ reaction on an iron target. The cross section of this reaction is at maximum when the incident $K^-$ momentum is 1.8 GeV/$c$ [25]. Thus, $K^-$ beam with 1.8 GeV/$c$ was used. The produced $\Xi^-$s were slowed down and stopped in the target. Then, they were captured by Fe atoms and $\Xi^-$Fe atoms were formed. The captured $\Xi^-$ hyperon transits to lower atomic orbits with X-ray emission, and the $\Xi^-$ hyperon is eventually absorbed by the nucleus.

For tagging the $p(K^-, K^+)\Xi^-$ reaction, particle identification and momentum analysis of the beam $K^-$ and the scattered $K^+$ are performed by K1.8 beam line and KURAMA spectrometer, respectively. In addition, X rays from $\Xi^-$ atoms were detected by a Ge detector array, Hyperball-X' surrounding the target. In this chapter, details of the experimental components are described.

## 2.2 J-PARC and K1.8 beam line

J-PARC is a high intensity proton accelerator facility. In this facility, the primary proton beam is accelerated up to 30 GeV by MR synchrotoron and extracted to HD for hadron experiments. In this experiment, the duration time of the proton beam was 2 seconds in 5.2-second repetition cycle. $2.5 \times 10^{13}$ protons per spill were irradiated to a primary gold target and secondary beams such as $K$, $\pi$ were produced. As shown in Fig. 2.1, the K1.8 beam line consists of several dipole, quadrupole and sextapole magnets. Secondary beam momentum was selected by dipole magnets and momentum slits. The contamination of secondary particles, mainly $\pi^-$, was rejected by two electrostatic separators (ESS1,2) and mass slits (MS1,2). The ESS1 and ESS2 were operated applying ±250 kV to a 10-cm gap. Beam tuning was carried out in order to maximize $\Xi^-$ production yield considering the $K^-$ intensity with a reasonable $K^-/\pi^-$ ratio. In data-taking period, a typical $K^-$ intensity was $4.5 \times 10^5$ per spill and a $K^-/\pi^-$ ratio was $\sim 7$ for 1.8 GeV/$c$. A typical beam profile at the iron target is shown in Fig. 2.2.

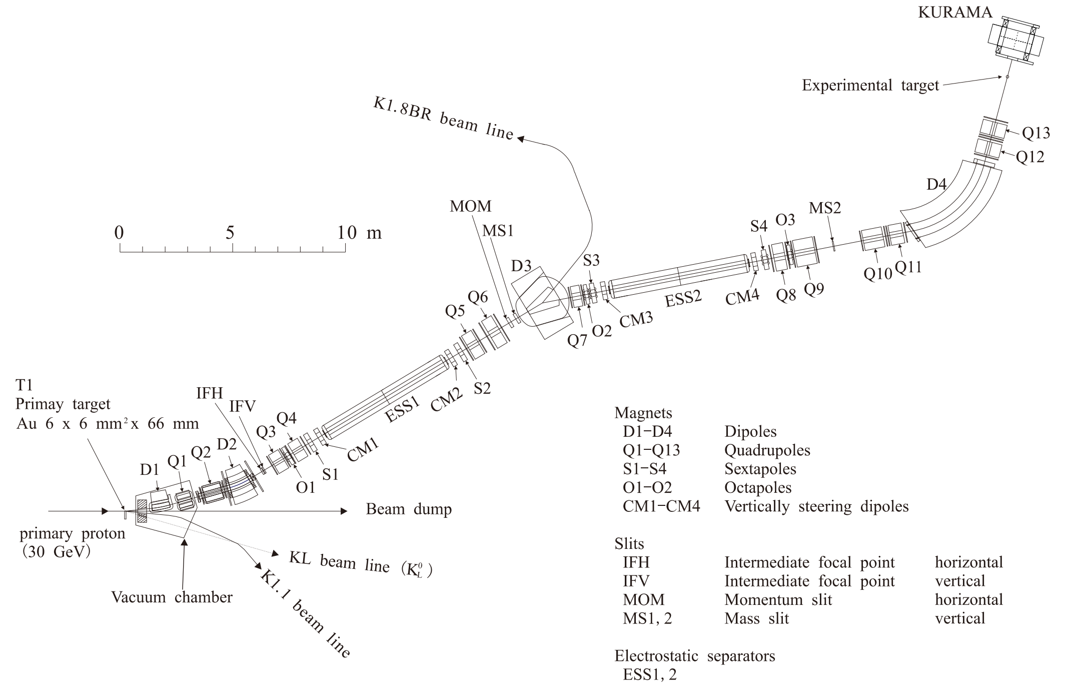

Figure 2.1: Schematic view of the K1.8 beam line.

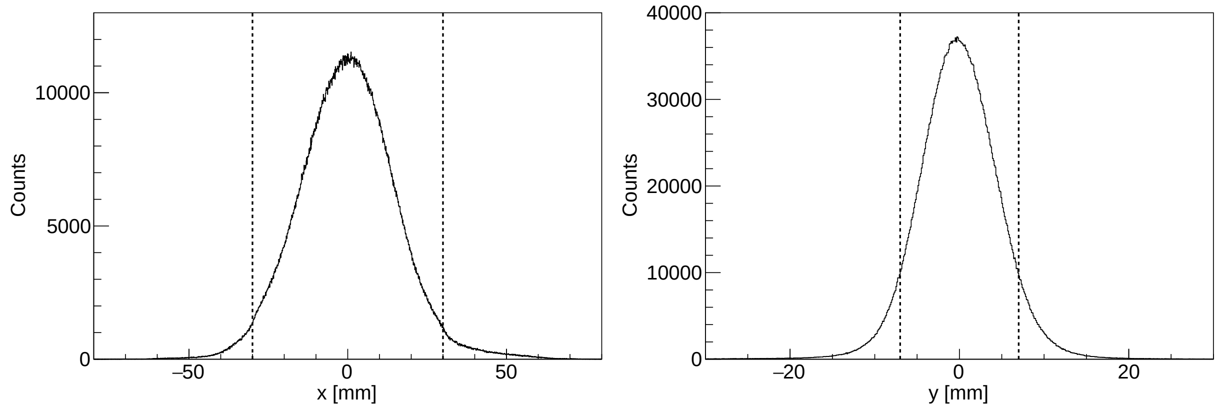

Figure 2.2: Typical beam profile along horizontal (x) and vertical (y) directions at the iron target. Dotted lines shows the actual target size.

## 2.3 K1.8 beam line spectrometer

The K1.8 beam line spectrometer was used for particle identification and momentum analysis of beam particles. The spectrometer consists of QQDQQ magnets, detectors for particle identification, and tracking detectors. Figure 2.3 shows schematic view of the K1.8 beam line spectrometer. To identify the beam particles, time-of-flight between two timing counters of plastic scintillation hodoscopes, BH1 and BH2, was measured. In addition, to reject contamination of pions in the beam at the trigger level, two aerogel Čerenkov detectors (BAC1 and BAC2) were installed. For momentum analysis, the beam position at upstream of the magnets and the beam track at downstream of the magnets were measured by fiber detector (BFT) and drift chambers (BC3 and BC4), respectively. The design value of the momentum resolution was $\Delta p/p = 3.3 \times 10^{-4}$ (FWHM) with a position resolution of 200 $\mu$m (rms). The magnetic field of the dipole magnet (D4) was monitored during the experiment with a hall probe. Table 2.1 lists design specifications of the K1.8 beam line spectrometer.

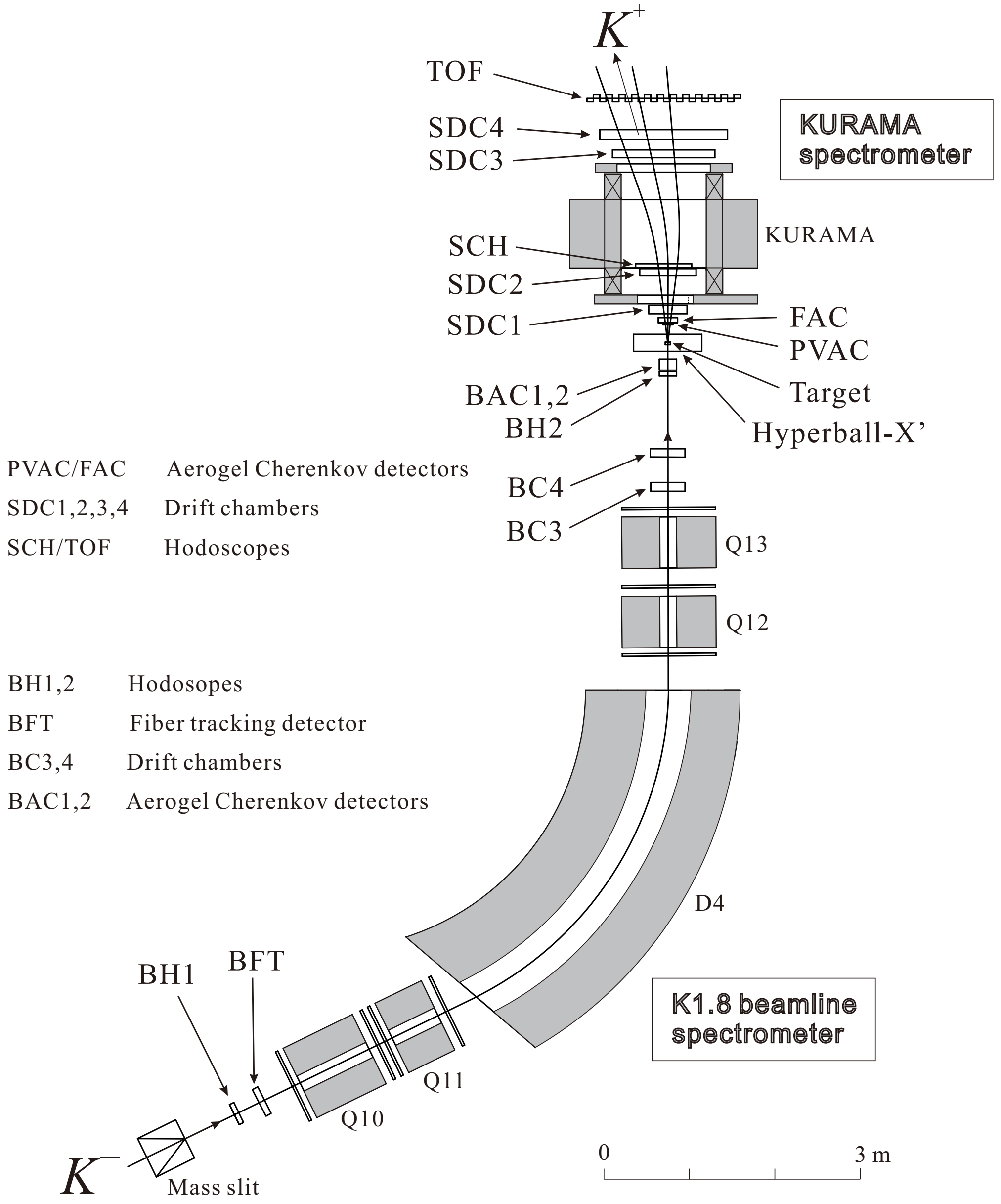

Figure 2.3: Schematic view of the K1.8 beam line and the KURAMA spectrometer for the J-PARC E03 experiment.

Table 2.1: Specifications of the K1.8 beam line spectrometer.

| | |
|---|---|
| Momentum resolution | $3.3 \times 10^{-4}$ (FWHM) |
| Maximum momentum | 2.0 GeV/$c$ |
| Momentum bite | ±3% |
| Bending angle | 64° |
| Flight length from BH1 to BH2 | 10 m |

### Counters for particle identification

#### BH1 and BH2

Two Beam Hodoscopes, BH1 and BH2, were installed at the entrance and the exit of the K1.8 beam line spectrometer. BH1 consisted of 11 segments of 5-mm-thick plastic scintillator and its effective area was $170^x \times 66^y$ mm. Photomultiplier tubes (PMT) were connected on both ends of each scintillator segment. BH2 consisted of 5 segments of 8-mm-thick plastic scintillator and its effective area was $111^x \times 50^y$ mm. For BH2, a PMT was mounted only on bottom side of each scintillator segment.

#### BAC1 and BAC2

Two Beam Aerogel Čerenkov counters (BAC1,2) were installed at the upstream of the target to select beam kaons in the trigger level. The two BACs were used to reduce misidentifying pions as kaons. The radiator was silica aerogel with a $170^x \times 57^y \times 66^z$ mm$^3$ area for each BAC. The reflective index of the radiator was 1.03, corresponding to the threshold momentum of 0.6 GeV/$c$ for pion and 2.0 GeV/$c$ for kaon. Three 2 ” fine-mesh type PMTs, Hamamatsu H6614-70UV, were connected to the radiator of each BAC directly.

Table 2.2: Specifications of the counters for beam particle identification.

| | Effective area ($W \times H \times T$[mm]) | Scintillator/Radiator | PMT made by Hamamatsu |
|---|---|---|---|
| BH1 | $170 \times 66 \times 5$ | Plastic scintillator: BC-420 | H6524MOD |
| BH2 | $111 \times 50 \times 8$ | Plastic scintillator: | H6524MOD |
| BAC1 | $160 \times 57 \times 66$ | Silica aerogel, n = 1.03 | H6614-70UV |
| BAC2 | $160 \times 57 \times 66$ | Silica aerogel, n = 1.03 | H6614-70UV |

### Tracking detectors

#### BFT

Scintillation fiber counter (BFT) [26] was located upstream of the QQDQQ magnets to measure the x position of incident beam particles. BFT consisted of 320 scintillation fibers with 1 mm diameter arranged horizontally in two layer (xx’) and the effective area was $160^x \times 80^y$ mm$^2$. A Multi-Pixel Photon Counter (MPPC) was attached to one end of each fiber directly for photon detection. For the operation and signal readout of the multi-MPPCs, electronics modules using EASIROC chips were used. The EASROC havs various functions such as bias adjustment, amplifier, shaper, discriminator and ADC.

#### BC3 and BC4

Two multi-wire drift chambers (BC3, BC4) were installed at the downstream of the QQDQQ magnets. Each chamber had six layers (xx'uu'vv'). The u and y layers were tilted by 15° and $-15°$, respectively. The drift length of both BC3 and BC4 was 1.5 mm. Mixed gas of Ar:iso-$C_4H_{10}$:Methylal = 76:20:4 was used.

Table 2.3: Specifications of BFT.

| | Effective area ($W \times H$[mm]) | Scintillator | MPPC made by Hamamatsu |
|---|---|---|---|
| BFT | $160 \times 80$ | Scintillation fiber, $\phi = 1$ mm<br>Kuraray SCSF-78M | S10362-11-100P |

Table 2.4: Specifications of BC3 and BC4.

| | Effective area ($W \times H$[mm]) | Planes | Tilt angle [deg] |
|---|---|---|---|
| BC3 | $192 \times 100$ | xx'vv'uu' | 0, -15, 15 |
| BC4 | $192 \times 100$ | uu'vv'xx' | 15 -15 0 |

## 2.4 KURAMA spectrometer

The KURAMA spectrometer was used for particle identification and momentum analysis for scattered particles. The spectrometer consisted of the KURAMA magnet, the detectors for particle identification (PVAC, FAC, SCH, TOF) and tracking detectors (SDC1-4) as shown in Fig. 2.3.

### Counters for particle identification

**PVAC and FAC**

Proton Veto Aerogel Čerenkov coutnter (PVAC) was installed at downstream of the iron target to reject scattered protons. The radiator of PVAC is silica aerogel with the reflective index of 1.12 and the effective area was $117^x \times 117^y \times 14^z$ mm$^3$. The threshold momentum for proton is 1.86 GeV/$c$. Four fine mesh PMTs were connected on the top and bottom of the radiator.

Forward Aeroge Čerenkov counter (FAC) was installed at just downstream of the PVAC to reject passing beam kaons and scattered pions. The radiator of FAC was silica aerogel with the reflective index of 1.05 and the effective area was $225^x \times 162^y \times 60^z$ mm$^3$. The threshold momentum for kaon is 1.54 GeV/$c$. Six fine mesh PMTs were connected on the top and bottom of the radiator.

**SCH**

Scattered Charge Hodoscope (SCH) was placed at downstream of SDC2 in the KURAMA magnet. SCH joined a matrix trigger to select events with the scattered particle of $K^+$. The detail of the matrix trigger is described in Sec. 2.6. SCH consisted of 64 plastic scintillators with 2-mm thickness and the effective area was $673^x \times 450^y$ mm$^2$. A wavelength shifting fiber with a diameter of 1 mm was embedded in each plastic scintillator and a MPPC was attached to one end of each fiber directly. The EASIROC system was used for signal readout of the MPPCs in the same way as BFT.

**TOF**

Time-Of-Flight wall (TOF) was installed at the most downstream of the KURAMA spectrometer to measure the time-of-flight between BH2 and TOF. TOF was composed of 24 plastic scintillators with 30-mm thickness and the effective area was $1805^x \times 1800^y$ mm$^2$. PMTs were mounted on both ends through acrylic light guides.

Table 2.5: Specifications of the counters for particle identification.

| | Effective area ($W \times H \times T$[mm]) | Scintillator/Radiator | PMT or SiPM made by Hamamatsu |
|---|---|---|---|
| PVAC | $117 \times 117 \times 14$ | Silica aerogel, n = 1.12 | R6682 |
| FAC | $225 \times 162 \times 60$ | Silica aerogel, n = 1.05 | R6682 |
| SCH | $673 \times 450 \times 2$ | Plastic scintillator: EJ-212 | S10362-11-100P |
| TOF | $1805 \times 1800 \times 30$ | Plastic scintillator: EJ-210 | H1949 |

Table 2.6: Specifications of SDCs.

| | Effective area ($W \times H$[mm]) | Planes | Tilt angle [deg] |
|---|---|---|---|
| SDC1 | $384 \times 264$ | uu'xx'vv' | 15, 0, -15 |
| SDC2 | $715 \times 430$ | xx'yy' | 0, 90 |
| SDC3 | $1152 \times 1152$ | xx'yy' | 0, 90 |
| SDC4 | $1920 \times 1280$ | yy'xx' | 90, 0 |

## Tracking detector

**SDC1-4**

Four Scattered Drift Chambers (SDCs) with drift cells of honeycomb structure were used in the KURAMA spectrometer. SDC1 and SDC2 were installed at upstream of the KURAMA magnet. The drift lengths of SDC1 and SDC2 were 3 mm and 5 mm, respectively.

SDC1 had six layers (uu’xx’vv’) and SDC2 had four layers(xx’yy’). The u and v layers were tilted by 15° and $-15°$, respectively. The gas mixture of both SDC1 and SDC2 was the same as BCs.

SDC3 and SDC4 were installed at downstream of the KURAMA magnet. The drift lengths of SDC3 and SDC4 were 4.5 mm and 10 mm, respectively. SDC3 and SDC4 consisted of four layers each (xx’yy’). The gas mixture of Ar:$C_2H_6$ = 50:50 was used for SDC3 and SDC4.

## 2.5 Germanium detector array - Hyperball-X’

Figure 2.4 shows the schematic view of the Ge detector array called Hyperball-X’. It consists of four Ge and BGO detector units. For energy calibration of Ge detectors, two LSO($Lu_2SiO_5$) scintillators and two $^{22}$Na sources were installed.

### 2.5.1 Ge detectors

Four clover-type Ge detectors were installed around the iron target. The clover-type detector made by EURISYS has four coaxial n-type Ge crystals arranged like a four-leaf clover. The active volume in the clover-type detector is about 470 cm$^3$ and the relative efficiency with respect to a $\phi$3”×3” NaI(Tl) detector is ~80%.

In this experiment using a high-energy secondary beam, high-energy charged particles pass through the Ge detectors. In such a high-energy deposit environment, a resistive-feedback type preamplifier can not be used due to saturation of the output signal. Thus, each Ge detector was equipped with a transistor-reset type preamplifier. The transistor-reset type preamplifier discharges when the output voltage exceeds a certain threshold value, restoring the voltage to the baseline. After the reset, a dead time of several hundred microseconds occurs due to a rapid distortion of shaping amplifier output voltage.

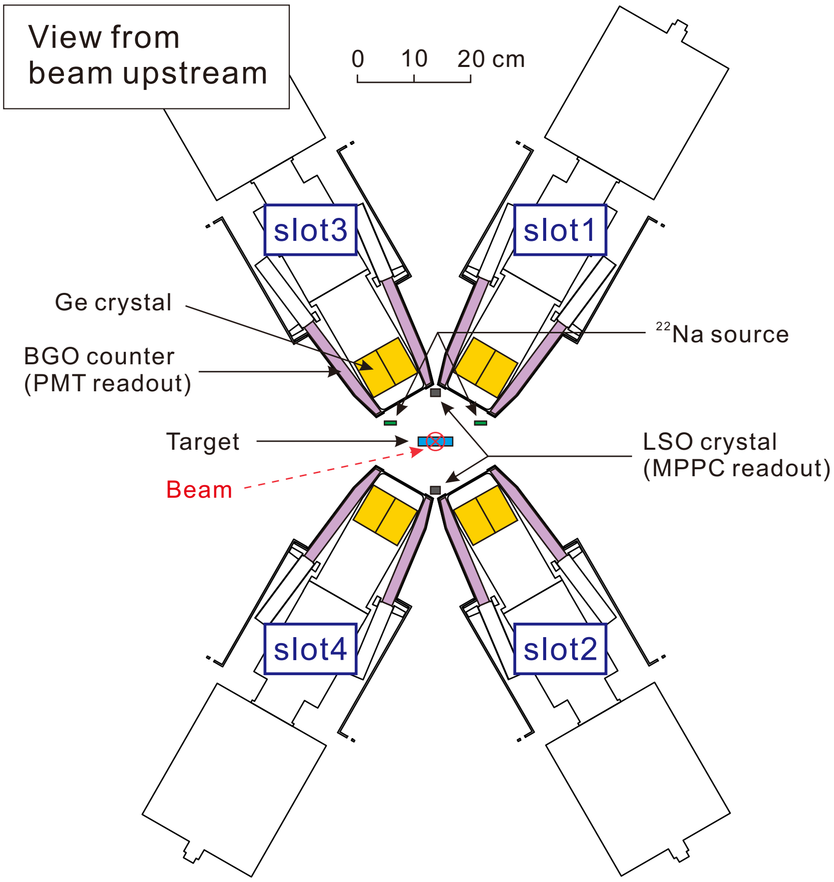

Figure 2.4: Schematic view of Hyperball-X’.

### 2.5.2 BGO detectors

Each clover-type Ge detector was surrounded by BGO detectors for background suppression. One BGO detector consisted of twelve $Bi_4Ge_3O_{12}$ crystals and 9/8” PMT was attached to each crystal. Background events were made by Compton scattering in the Ge detector, high energy gamma rays from $\pi^0$ decay and high-energy charged particles caused by beam. Figure 2.5 shows a schematic view of the Ge crystals and BGO crystals for a single unit of the detectors. The coincidence events between one Ge crystal and at least one of the four BGO crystals closest to it were rejected for the background suppression.

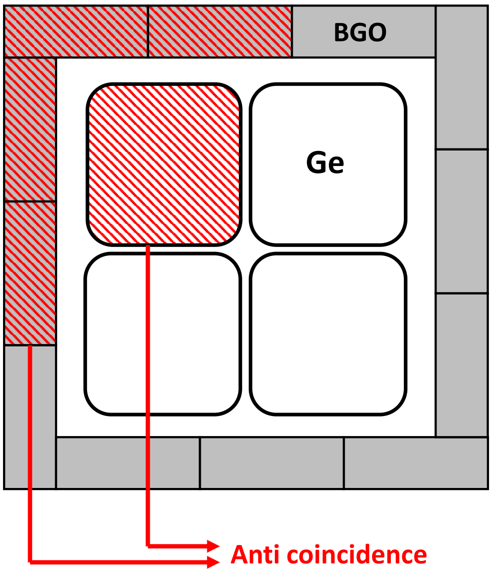

Figure 2.5: Schematic view of the Ge crystals and BGO crystals for a single unit of the detectors.

### 2.5.3 Readout system for Hyperball-X’

Figure 2.6 shows a diagram of readout system for Hyperball-X’. The preamplifier output signal of the Ge detector was divided into two lines, one for energy information and the other for timing information. A fast Timing Filter Amplifier (TFA, ORTEC 579) was used for reading out timing information. The TFA output signal was sent through a Constant Fraction Discriminator (CFD, ORTEC 934) to HUL Multi-Hit TDC (MHTDC). HUL (Hadron Universal Logic) is a general purpose logic module with an FPGA [27]. ORTEC 671 shaping amplifier was used to read out energy information. Considering energy resolution and deadtime, the shaping time was set to 3 $\mu$s. The output signal was digitized by a peak-sensitive ADC with a 13 bit resolution (ORTEC AD413A). The ADC data from AD413A module were sent through FERA driver to HUL UMEM-Eumulator introduced for the first time in this experiment. The module implements the functionality of a Universal MEMory module (UMEM) used in previous experiments in the firmware of HUL module. The shaping amplifier also output a timing signal called Count-Rate-Monitor (CRM) signal. To reject the events several hundred microseconds after the preamplifier reset, the reset timing signal from preamplifier was sent to HUL Reset Timing Recorder (RTR), which we developed for this experiment. HUL RTR has 28-bit counter circuits running with a 10 MHz clock and a reset timing signal from the preamplifier was used for counter reset. In addition, counter values was recorded when the trigger signal was input. Thereby, the elapsed time from the last reset timing of the preamplifier to the timing of trigger generation was obtained with 100 ns timing resolution. For the BGO detector, only TDC data were taken. The PMT signals were discriminated by a CAEN V895 module and sent to a HUL MHTDC.

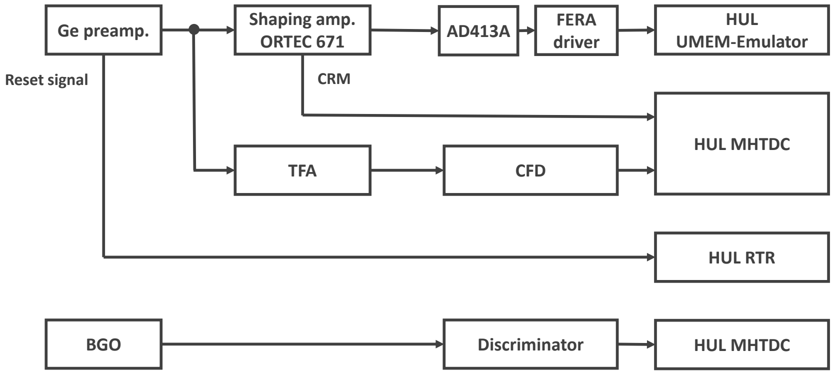

Figure 2.6: Diagram of the readout system for Hyperball-X’.

### 2.5.4 Energy calibration system

For the energy calibration of Ge detectors, LSO($Lu_2SiO_5$) scintillation counters and $^{22}$Na sources were used. This calibration system was originally developed for the previous experiment (J-PARC E07) to measure the $\Xi^-$ atomic X-ray energy shift which is expected to be 0.3 keV [28]. The performance of this system was also sufficient for the present experiment.

Two $Lu_2SiO_5$ scintillators were installed as shown in Fig. 2.4. The crystal contains natural activity of $^{176}$Lu which emits 202 keV and 307 keV $\gamma$ rays after beta decay. The clear reference peaks were obtained even in the on-beam period by $\beta - \gamma$ coincidence measurement between the LSO counter and the Ge detector. The upper LSO counter was for SLOT 1 and 3. Also, the lower one was for SLOT 2 and 4. The scintillation light from the LSO crystal was detected by a MPPC.

Two $^{22}$Na sources were also installed in order to cover the energy region up to 500 keV. $^{22}$Na emits two back-to-back 511 keV $\gamma$ rays after $\beta^+$ decay followed by electron-positron annihilation. The beam-induced 511 keV $\gamma$ ray peak was also produced. However, it was not usable because its shape was distorted and broadened. The clear 511 keV $\gamma$ ray peak from $^{22}$Na was obtained by coincidence measurement between a pair of the Ge detectors. As shown Fig. 2.4, the $^{22}$Na source on the right-hand side was for the pair of SLOT 1 and 2. Also, one on the left-hand side was for SLOT 3 and 4. In this experiment, calibration data with the $^{22}$Na source was taken, but the data was not used for the present analysis focusing on the energy region of 100-400 keV. Therefore, only two reference points, 202 and 307 keV from $^{176}$Lu were used for the energy calibration.

## 2.6 Trigger

### 2.6.1 $(K^-, K^+)$ reaction trigger

Figure 2.7 shows the trigger logic diagram for the $(K^-, K^+)$ reaction. In the trigger logic, teh beam kaon ($K_{in}$) and the scattered kaon ($K_{out}$) were defined as follows.

$$K_{in} \equiv \mathrm{BH2} \times \overline{\mathrm{BAC1}} \times \overline{\mathrm{BAC2}} \tag{2.1}$$

$$K_{out} \equiv \mathrm{PVAC} \times \overline{\mathrm{FAC}} \times \mathrm{TOF} \tag{2.2}$$

The pion contamination in the kaon beam was rejected by using BAC1 and BAC2 as veto counters. Scattered protons were rejected by PVAC. Scattered pions and passing beam particles were also rejected by FAC. In addition, the matrix coincidence trigger (MATRIX) joined the $(K^-, K^+)$ reaction trigger for more efficient selection. The matrix consisted of hit patterns of three hodoscopes, BH2, SCH and TOF. There were two kinds of matrix pattern. One was two-dimensional matrix (2DMATRIX), which selected scattered $K^+$ using SCH and TOF. The other was three-dimensional matrix (3DMATRIX), which rejected beam particle passing through using BH2, SCH and TOF. The triggers of MATRIX and $(K^-, K^+)$ reaction (KK) were defined as follows.

$$\mathrm{MATRIX} \equiv \mathrm{2DMATRIX} \times \overline{\mathrm{3DMATRIX}} \tag{2.3}$$

$$KK \equiv K_{in} \times K_{out} \times \mathrm{MATRIX} \tag{2.4}$$

Figure 2.8 shows the hit combination between SCH and TOF segments for data obtained by the KK trigger without 2DMATRIX. The trigger rate of $K_{in} \times K_{out}$ was around 170 k/spill. The trigger rate was reduced to 3.5 k/spill by adding the MATRIX trigger. The signal from each detector was sent to the HUL modules to produce the logic signals in Eq. 2.1-2.4.

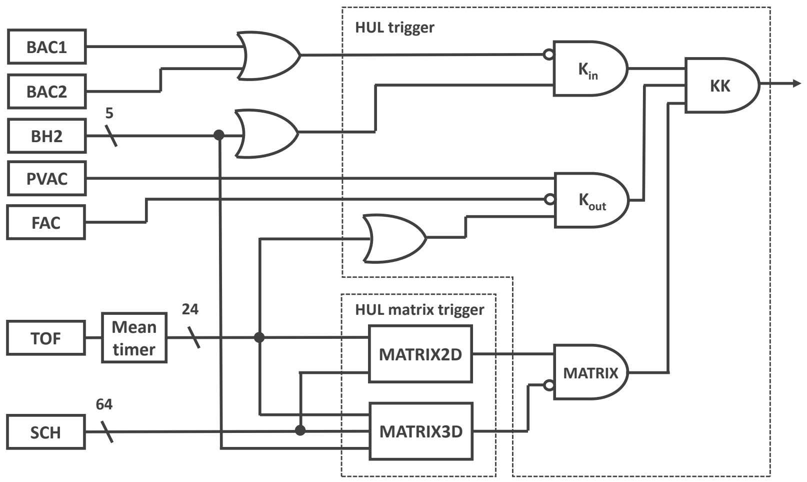

Figure 2.7: Trigger logic diagram for the $(K^-, K^+)$ rection.

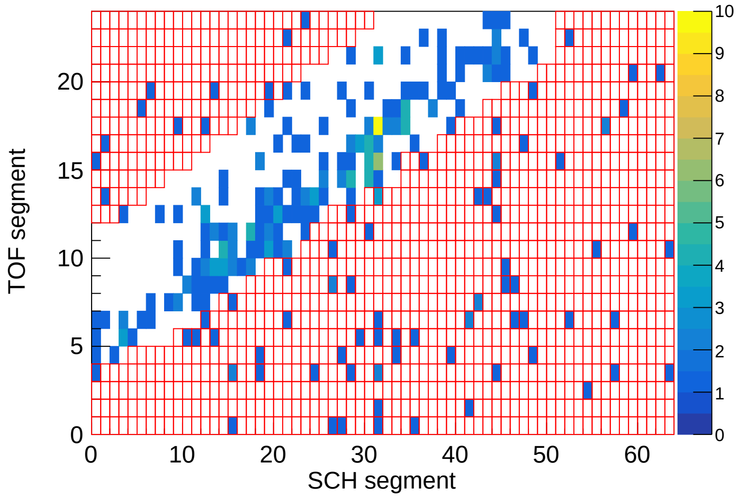

Figure 2.8: Hit combination between SCH and TOF segments for data obtained by the KK trigger without 2DMATRIX. In this distribution, the scattered particles identified as $K^+$ by the data analysis were used. The area not surrounded by red blocks was accepted.

### 2.6.2 Triggers for Ge detectors

The energy calibration data for Ge detectors were taken in both on-beam-spill and off-beam-spill periods. There were two triggers, Ge-LSO coincidence trigger(Ge×LSO) for $\gamma$ rays from $^{176}$Lu and Ge-Ge coincidence trigger(Ge×Ge) for back-to-back $\gamma$ rays from $^{22}$Na. For Ge×LSO trigger, the lower and upper thresholds of LSO counters were set in order to reject the false signal due to MPPC dark current and beam-induced high energy particles. With these coincidence trigger, the clean spectra for energy calibration were obtained even in high counting rate environments.

### 2.6.3 Summary of trigger

Table 2.7 shows the rate of each trigger. Data of BH2 trigger and BH2×TOF×$\overline{\text{3DMATRIX}}$ were taken for monitoring of the detector performance.

Table 2.7: Summary of trigger rates.

| Trigger | | BH2 | BH2×TOF×$\overline{\text{3DMATRIX}}$ | KK | Ge×LSO | Ge×Ge |
|---|---|---|---|---|---|---|
| Beam on | Rate [k/spill] | 0.1 | 0.1 | 3.5 | 1.5 | 1.5 |
| | Prescale factor | 6000 | 480 | 1 | 2 | 8 |
| Beam off | Rate [k/spill] | - | - | - | 1.5 | 1.5 |

## 2.7 Data acquisition system

Several types of readout systems such as VME, EASIROC, HUL were used in the experiment. To integrated readout of the subsystems, a network-based software, Hadron DAQ (HDDAQ) usning TCP/IP protocol and a trigger/tag distribution sysytem with Master Trigger Module (MTM) were used [29]. Figure 2.9 shows a scheme of the DAQ system. MTM sent a trigger and a event tag to each subsystems. The trigger was used for a gate of the ADC and a common stop signal for the TDC. Data of the subsystems was tagged with spill and event number. In addition, MTM was received a busy signal from each subsystems. MTM accepted a trigger in the spill gate corresponding to beam-extraction time while a busy state was off. Thereby, the consistency of the event number of all the subsystems was monitored.

In the VME subsystem, QDC modules (CAEN V792) were used to digitize energy deposit information of BH1, BH2, TOF, and ACs. The digitized data were transferred to a VME-CPU module as a front-end computer. The hit timing information of BFT and SCH was digitized in the EASIROC modules. In the HUL subsystem, HUL High-resolution Multi-Hit TDC was used for hit timing information of BH1, BH2, TOF, and ACs. HUL MHTDC was used for hit timing information of all the wire chambers, the Ge detectors and the BGO detectors. Furthermore, HUL UMEM-Emulator and HUL RTR were used to obtain the energy information and the preamplifier reset timing of the Ge detectors, respectively. EASIROC and HUL transferred the data to front-end computers with SiTCP communication.

The event builder of the host computer collected the data of each fornt-end and built an event one by one. Then, the built data was sent to online analyzer and file server via event distribution. The controller of the host computer managed the event builder, the event distributor, the recorder and each subsystems. A typical DAQ efficiency was 90% with a trigger rate of 10 k/spill.

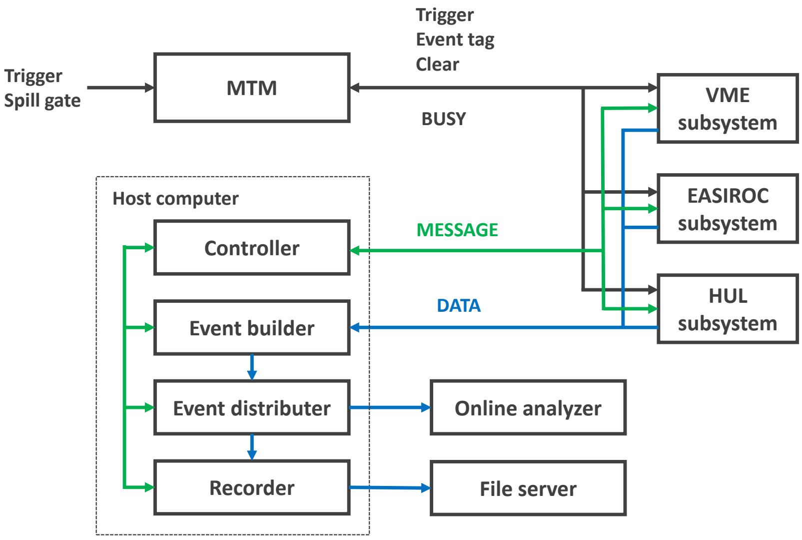

Figure 2.9: The scheme of DAQ system.

## 2.8 Target

An iron target was installed between the beam line spectrometer and the KURAMA spectrometer. The thickness of the target was 23.6 g/cm$^2$ and the size was $60^x \times 14^y \times 30^z$ mm$^3$. The size was optimized considering the beam profile, the cross section of the $(K^-, K^+)$ reaction, $\Xi^-$ stopping probability and X-ray self absorption. In a calibration run, a polyethylene target with a 9.5 g/cm$^2$ thickness was used.

## 2.9 Data summary

The data taking was performed in 2020 and 2021. The iron target was irradiated with a total of $9.5{\times}10^{10}$ beam $K^-$ in 20 days. For the calibration run, the polyethylene target was irradiated with $9.0{\times}10^8$ beam $K^-$ in total.

# Chapter 3

# Analysis

## 3.1 Overview

The procedure of data analysis to obtain the $\Xi^-$ atomic X-ray spectrum is shown in Fig. 3.1. The analysis to select the $(K^-, K^+)$ reaction is described in Sec. 3.2. Beam $K^-$s and scattered $K^+$s were analyzed by the beam line spectrometer and the KURAMA spectrometer, respectively. The missing mass of the $p(K^-, K^+)X$ reaction was reconstructed to select the $\Xi^-$ production event. To obtain a good signal to noise ratio, an additional analysis selecting $\Xi^-$ with a large stopping probability was performed using measured missing momentum described in Sec. 3.4. The analysis of Hyperball-X' to obtain the X-ray spectrum is described in Sec. 3.3. Event selection was performed by using the timing information of the Ge detectors and the BGO counters. In addition, the ADC data of the Ge detectors was calibrated by using data obtained with the Ge×LSO trigger, generated by the LSO counters.

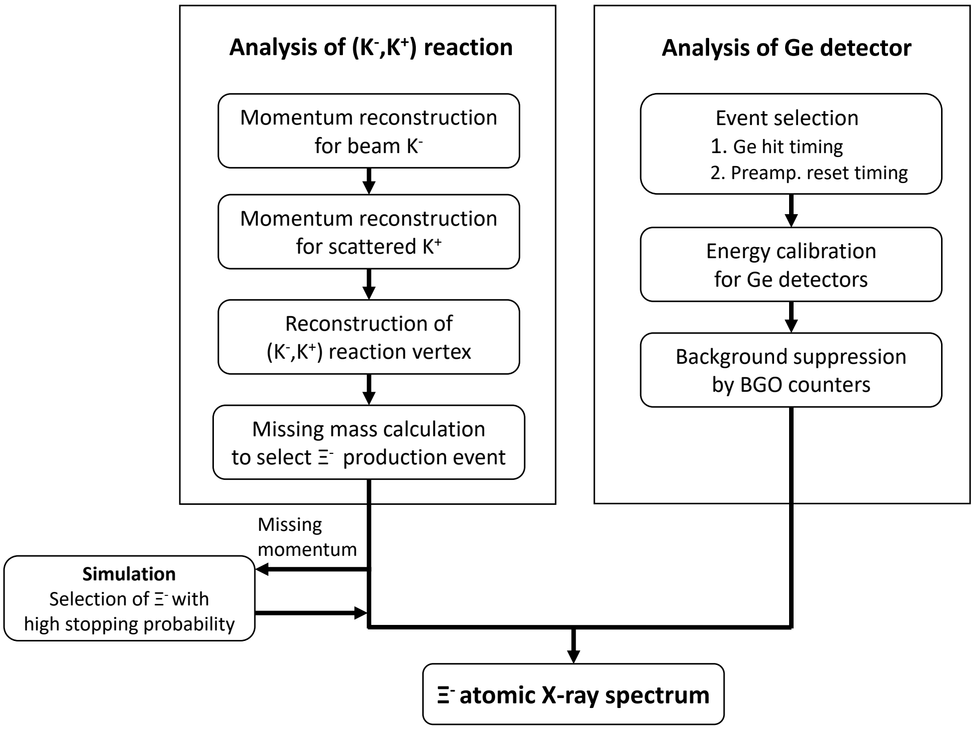

Figure 3.1: Procedure of data analysis.

## 3.2 Spectrometer analysis

### 3.2.1 Analysis for beam particles

**$K^-$ selection**

Figure 3.2 shows a distribution of time-of-flight between BH1 and BH2 for the KK trigger data. Since the $\pi^-$ time-of-flight was adjusted to 0 as a reference using the BH2 trigger data, the distribution represents a difference from the $\pi^-$ time-of-flight. The time-of-flight resolution was 0.195 ns ($\sigma$). $\pi^-$ mesons were rejected sufficiently by BAC1 and BAC2 in trigger level as shown in Fig 3.2. Therefore, in the offline analysis, the event selection was not applied for the beam time-of-flight.

**Momentum reconstruction for beam particles**

For momentum analysis, the horizontal positions of beam particles at the entrance of the QQDQQ magnets were measured using BFT. Figure 3.3 shows a timing distribution of BFT for $K^-$ beam. In addition, the trajectories of the beam particles at the exit of the QQDQQ magnets were reconstructed using hit positions of BC3 and BC4. A straight track was obtained with least chi-squared fitting. The fitting required hits on at least 10 out of 12 layers and there are four fitting parameters $(x, y, dx/dz, dy/dz)$. Chi-square was defined as

$$\chi^2 \equiv \frac{1}{n-4}\sum_{i=1}^{n}\left(\frac{s_i^{hit} - s_i^{track}}{\sigma_i}\right)^2, \tag{3.1}$$

where $n$ is the number of layers having hits, $s_i^{hit}$ and $s_i^{track}$ are hit position and calculated position from the track for the $i$-th layer, respectively, and $\sigma_i$ is position resolution of the $i$-th layer. The position resolutions were obtained from residual distributions in the fitting to be around 200 $\mu$m.

The moomenta of the beam particles were reconstructed using a third-order transfer matrix, $M$, as

$$\vec{X}_{in} = M(\vec{X}_{out},\ \delta) \tag{3.2}$$

$$\vec{X} = \left(x,\ y,\ \frac{dx}{dz},\ \frac{dy}{dz}\right). \tag{3.3}$$

The components of $\vec{X}$ are particel positions and directions with respect to the horizontal and vertical axes. $\vec{X}$ at the exit of the QQDQQ magnets was obtained by BC3 and BC4. For $\vec{X}$ at the entrance of the magnets, only a horizontal position, $x_{in}$ was measured with BFT. $\delta$ is the deviation from the central momentum and is obtained by solving a cubic equation, $x_{in} = f(\vec{X_{out}}, \delta)$. The central momentum was set to 1.81 GeV/$c$ from the monitor value of the magnetic field. Figure 3.4 shows a distribution of reconstructed momentum of the $K^-$ beam.

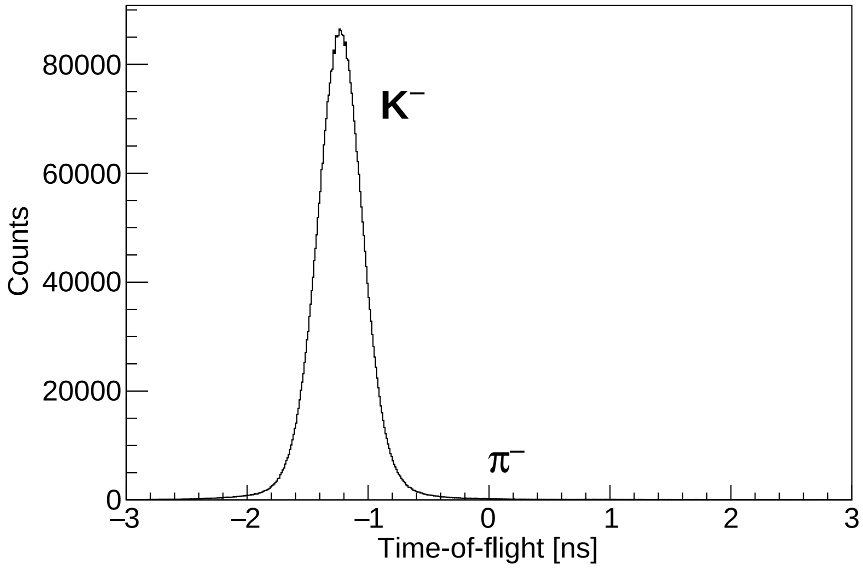

Figure 3.2: Timing distribution of the beam time-of-flight between BH1 and BH2.

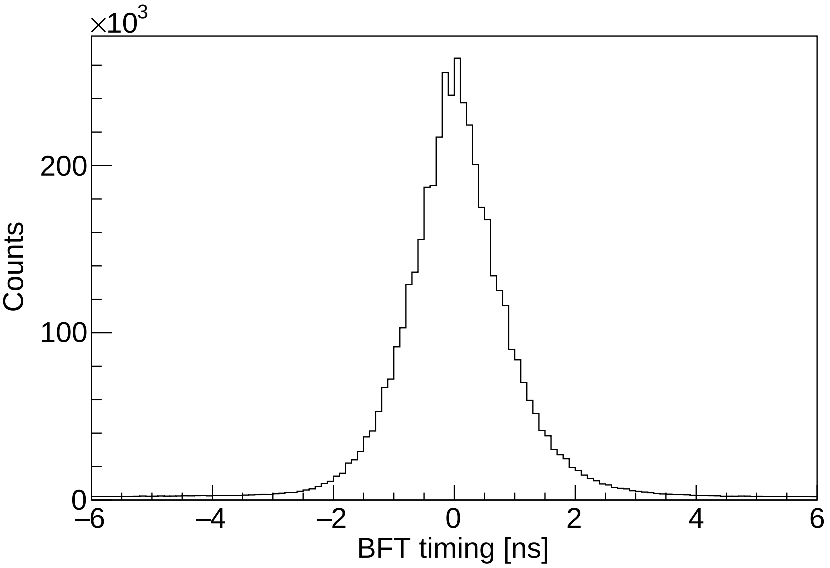

Figure 3.3: Timing distribution of the BFT.

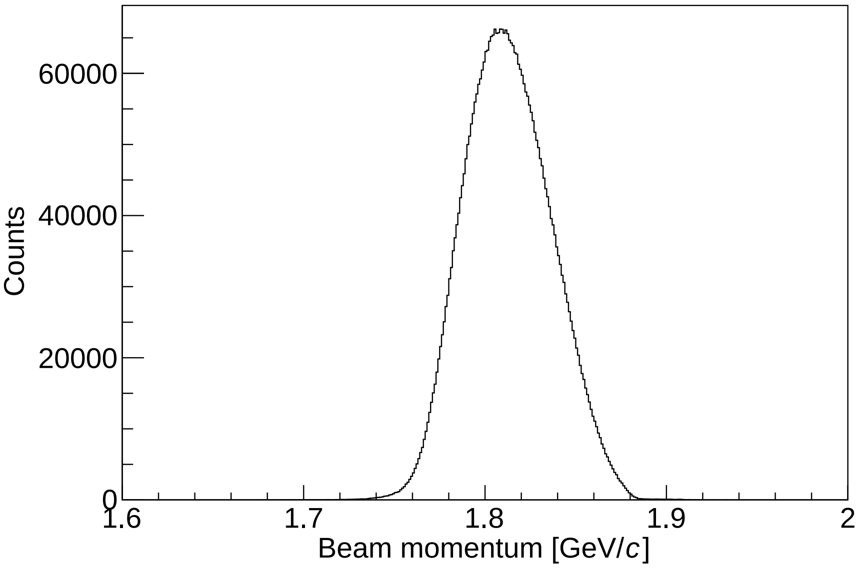

Figure 3.4: Reconstructed momentum distribution of beam $K^{-}$s.

### 3.2.2 Analysis for scattered particles

#### Momentum reconstruction for scattered particles

The tracks of scattered particles at the entrance and exit of the KURAMA magnet were used to reconstruct the momenta of the scattered particles. The tracks at the magnet entrance were obtained using the hit position of SDC1 and SDC2. On the other hand, the tracks at the magnet exit were obtained using TOF in addition to the hit positions of SDC3 and SDC4. The horizontal and vertical hit positions of TOF were calculated by using the position of the hit scintillator and the time difference between up and down PMT's signals, respectively. These local tracks were obtained using least chi-squared fitting in the same way as BC3 and BC4. The fitting required hits on at least 8 out of 12 layers and 6 out of 8 layers for SDC1,2 and SDC3,4, respectively.

The Runge-Kutta method [30] was used to reconstruct the trajectory of the scattered particle in KURAMA magnet. The trajectory was also obtained by the least chi-squared fitting (KURAMA tracking). The fitting parameters were horizontal and vertical positons and directions of a starting vector, and a particle charge divided by the momentum. The chi-square value was defined as

$$\chi^2 \equiv \frac{1}{n-5}\sum_{i=1}^{n}\left(\frac{s_i^{hit}-s_i^{track}}{\sigma_i}\right)^2, \tag{3.4}$$

where $n$, $s_i^{hit}$, $s_i^{track}$ and $\sigma_i$ were as same as for Eq. 3.1. The maximum number of $n$ was 22. The fitting was done assuming both negative and positive particle charges and the one with the better chi-square was selected. Figure 3.5 shows a chi-square distribution of the KURAMA tracking. Data with a KURAMA tracking chi-square of less than 50 were accepted.

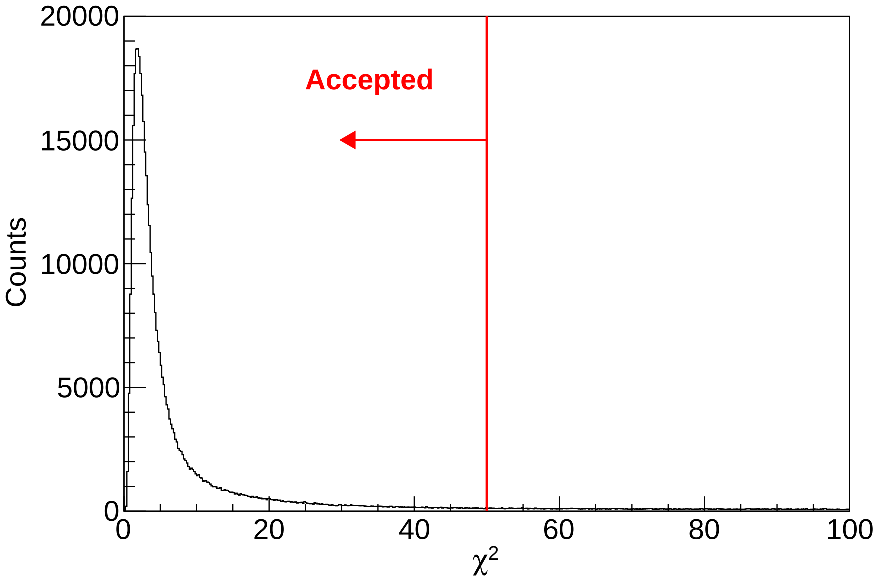

Figure 3.5: $\chi^2$ distribution of the KURAMA tracking.

### $K^+$ selection

The mass squared of the scattered particle was calculated as

$$M^2_{scat} = \left(\frac{p}{\beta}\right)^2 (1-\beta^2) \tag{3.5}$$

$$\beta = \frac{L}{Tc}, \tag{3.6}$$

where $p$ and $\beta$ are the reconstructed momentum and velocity, respectively. $L$ and $T$ are the flight path length and the flight time between the target and TOF, respectively. The flight time was obtained as time-of-flight between BH2 and TOF considering the distance between the target and BH2. Figure 3.6 shows the correlation between the mass squared and the momentum for scattered particles with a positive charge by applying the vertex cut as described in Sec. 3.2.3. The area surrounded by the red lines was accepted for selecting $K^+$. The particles with momenta higher than 1.3 GeV/$c$ and lower than 0.5 GeV/$c$ were rejected because protons and $\pi^+$s significantly contaminated the $K^+$ region were dominant, respectively. On the other hand, the squared mass within the $\pm 2\sigma$ region from the $K^+$ mass was accepted in consideration of signal to noise ratio.

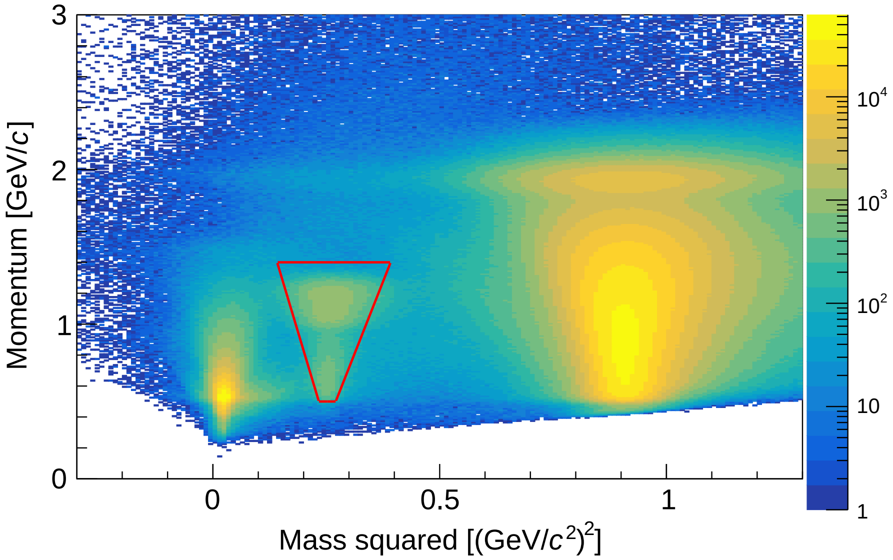

Figure 3.6: Correlation between the mass squared and the momentum for the scattered particles with a positive charge.

### 3.2.3 Identification of $(K^-, K^+)$ reaction

The $(K^-, K^+)$ reaction vertex was calculated as a closest distance between the tracks of the beam and scattered particles. The z axis of the vertex coordinator was defined as the beam axis. The origin of 3D vertex coordinators is the center position of the iron target. In addition, the scattering angle was defined as the angle between the vectors of the beam and scattered particles in the laboratory frame. Figure 3.7 and 3.8 show the z-vertex distribution and the correlation between the z-vertex and the scattering angle. The events with scattering angles of less than 3° were rejected because they often result in incorrect tracking or they have worse z-vertex resolution. Then, a z-vertex cut was applied to remove background due to reactions occurring outside the iron target. A $\pm 3\sigma$ region was selected assuming the distribution for the reaction in the target to be a Gaussian distribution. Figure 3.9 shows distributions of x and y positions of the vertex when the z-vertex cut was applied. The dashed lines in Fig. 3.7 and 3.9 indicate the actual target size. The x and y-vertex cut were applied with range of ±40, ±20 mm, respectively.

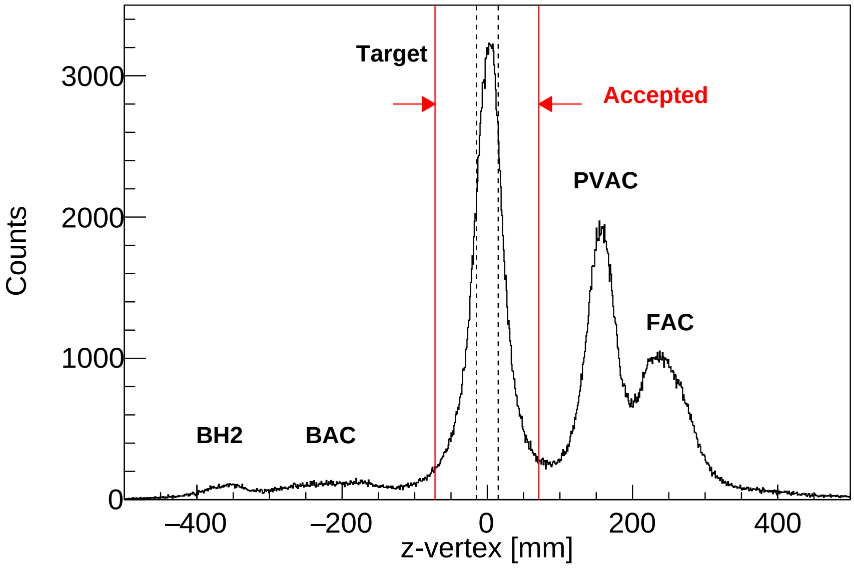

Figure 3.7: z-vertex distribution. Dotted lines shows the actual target size.

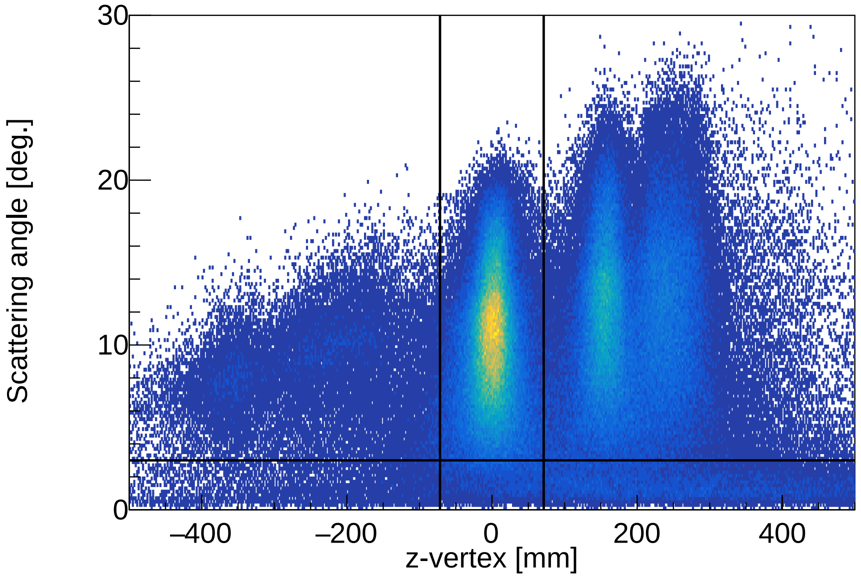

Figure 3.8: Correlation between the z-vertex and the scattering angle.

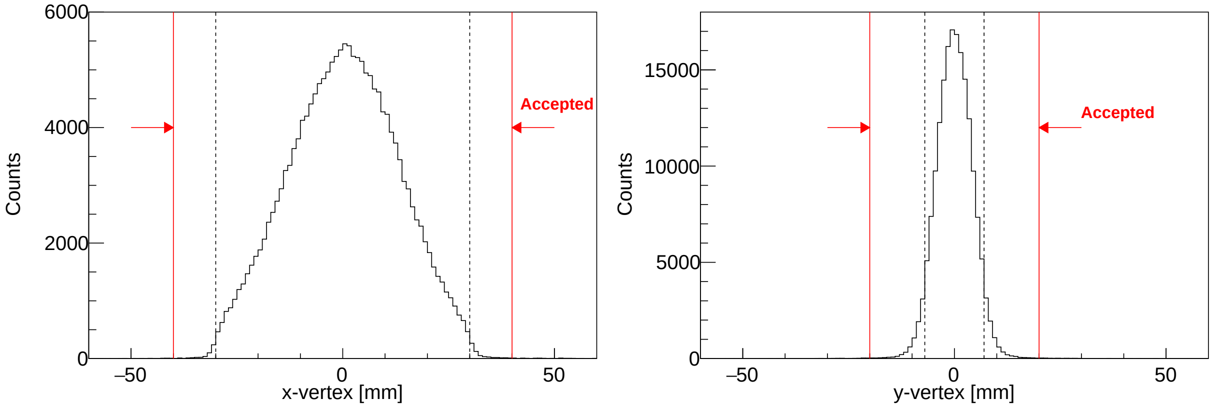

Figure 3.9: x and y-vertex distribution after when the z-vertex cut was applied. Dotted lines shows the actual target size.

### 3.2.4 Calculation of missing mass

The missing mass of the $p(K^-, K^+)X$ reaction was derived from the measured momenta of the beam $K^-$ ($p_{K^-}$) and the scattred $K^+$ ($p_{K^+}$), and scattring angle ($\theta$) as

$$M_X = \sqrt{(E_{K^-} + M_p - E_{K^+})^2 - (p_{K^-}^2 + p_{K^+}^2 - 2p_{K^-}p_{K^+}\cos\theta)}, \tag{3.7}$$

where $E_{K^-}$ and $E_{K^+}$ are total energies of the beam $K^-$, the scattered $K^+$ , respectively, and $M_p$ is the proton mass.

The missing mass of the $p(K^-, K^+)X$ reaction was calculated to select $\Xi^-$ production events. Figure 3.10 shows the missing mass spectrum calculated for the $p(K^-, K^+)X$

kinematics with the polyethylene target. The peak structure of $\Xi^-$ was observed with a missing mass resolution of 0.034 GeV/$c^2$ in FWHM. The distribution contained the components of $\Xi^-(1530)$, $\Xi\pi$ production and the contribution of the carbon target.

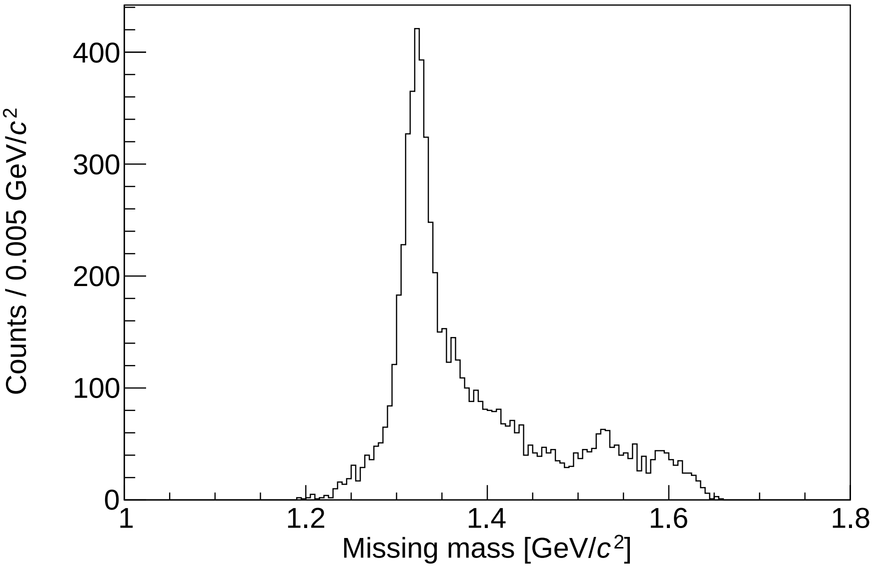

Figure 3.10: Missing mass spectrum calculated for the $p(K^-, K^+)X$ kinematics with the polyethylene target.

Figure 3.11 shows the missing mass spectrum caluclated for the $p(K^-, K^+)X$ kinematics with the iron target. The missing mass spectrum was broadened compared with that for the polyethylene target due to Fermi motion of the proton.

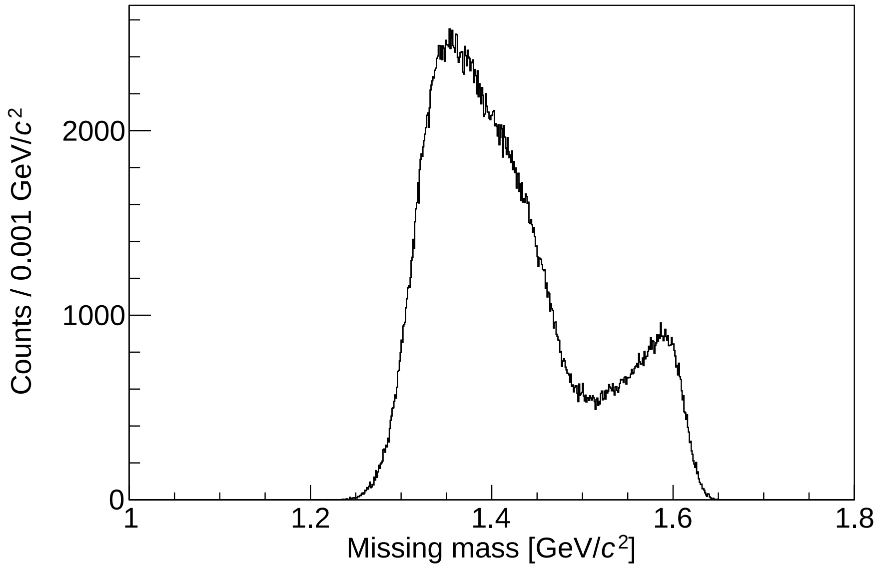

Figure 3.11: Missing mass spectrum for the $p(K^-, K^+)X$ kinematics with the iron target.

# 3.3 X-ray analysis

## 3.3.1 Event selection

### Event selection with Ge-hit timing

To select $\Xi^-$ atomic X rays, the events with coincidence of the Ge detectors and the KK trigger were selected in offline analysis. In the present experiment, two kinds of hit timing information of the Ge detectors were taken as shown in Fig. 2.6. One (CRM timing) was obtained by a CRM signal from ORTEC 671 shaping amplifier. The other (TFA timing) was obtained by TFA and CFD. The resolution of the TFA timing is better than the CRM timing. However, the CFD threshold of several channels could not be set low enough, namely, less than 100 keV. Thus, the CRM timing was also used. Figure 3.12 shows a typical correlation between the TFA timing and the measured energy of the Ge detectors for the KK trigger events. In the low energy region, the timing distribution had a correlation with the energy even using CFD. Therefore, an energy-dependent timing gate was applied as shown in Fig. 3.12. Figure 3.13 shows a typical TFA timing distribution of the Ge detectors for the measured energy of 100–400 keV. The timing gate for the CRM timing was also applied in the same way

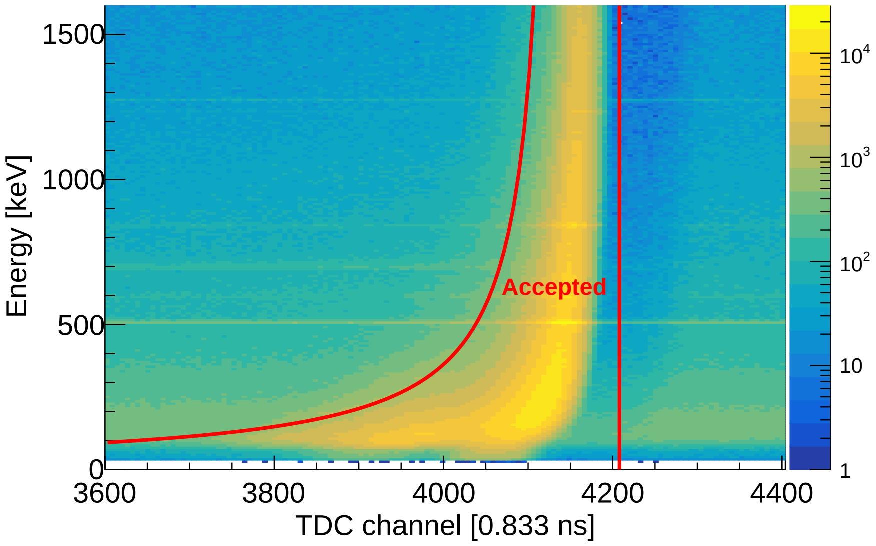

Figure 3.12: Typical correlation between the hit timing (TFA timing) and the measured energy of the Ge detectors for the $(K^-, K^+)$ trigger events.

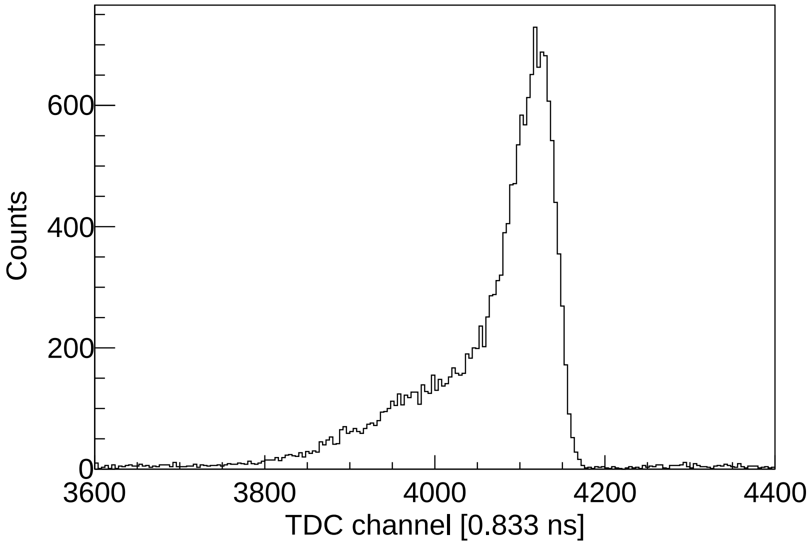

Figure 3.13: Typical hit timing (TFA timing) distribution of the Ge detectors for the measured energy fo 100–400 keV for the $(K^-, K^+)$ trigger events.

**Background suppression with preamplifier-reset timing**

The output voltage of the shaping amplifier is changed rapidly after the preamplifier reset. It takes several hundred microseconds for the output voltage to return to the baseline. Figure 3.14 shows a typical correlation between the elasped time from the last preamplifier reset to the trigger timing, and measured energy around the reference peak from $^{176}$Lu. Data for several hundred microseconds after the preamplifier reset was not used because the recorded energy information was not correct. The minimum elapsed time, corresponding to a red line in Fig. 3.14, was set for each Ge detector. For all the Ge crystals, the thresholds range from 500 to 6000 (50 - 600 $\mu$s).

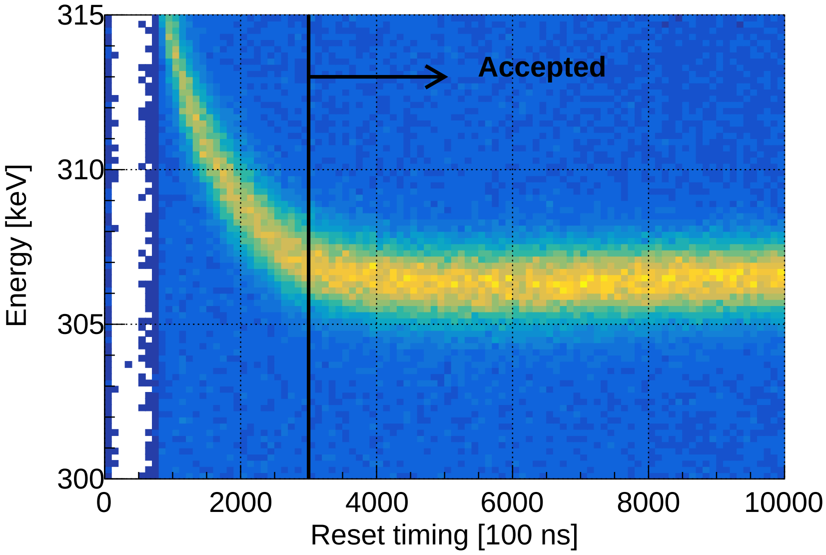

Figure 3.14: Typical correlation between the preamplifier reset timing and the measured energy around the reference peak from $^{176}$Lu. The data was taken with the LSO×Ge trigger in the beam-on period.

### Background suppression by BGO counters

Background in the energy spectrum of Ge detector was caused by Compton scattering, high energy gamma rays from $\pi^0$ decay and passage of high-energy charged particles. To suppress these events, anti-coincidence between the Ge detector and its surrounding BGO counter was taken. Figure 3.15 shows a typical timing distribution of BGO counters for the $(K^-, K^+)$ trigger events. Widening the anti-coincidence time gate increases the suppression efficiency, but also reduces the number of the real signal. The time gate was studied using the $\gamma$ ray of 212 keV from $^{54}$Mn in the $(K^-, p)$ reaction. This $\gamma$ ray was suitable for the study because it followed nuclear reaction and its energy was close to that of $\Xi^-$ atomic X ray. Figure 3.16 shows an energy spectrum of the Ge detectors for the $(K^-, p)$ reaction with and without the BGO suppression with the optimal time-gate width described below. Figure 3.17 shows a dependence of BGO time-gate width on peak survival ratio and accidental kill ratio for the $\gamma$ ray from $^{54}$Mn. The peak survival ratio was the ratio of peak counts before and after BGO suppression. The ratio was saturated around 0.7 with the time-gate width of more than 100 ns. Figure 3.18 shows the dependence of BGO time-gate width on peak significance ($S/\sqrt{S+N}$) for the $\gamma$ ray from $^{54}$Mn. The peak significance increased rapidly up to the time-gate width of 50 ns, and the increase was modest for time-gate width above 50 ns. The peak significance was maximized at time-gate width of 230 ns and applied for the spectrum of $\Xi^-$ atomic X ray. The background-suppression efficiency in the region of 200-300 keV was 69% and the peak survival ratio For the $\gamma$ ray from $^{54}$Mn was 70%. The same effect was expected for the X rays from $\Xi^-$ atom.

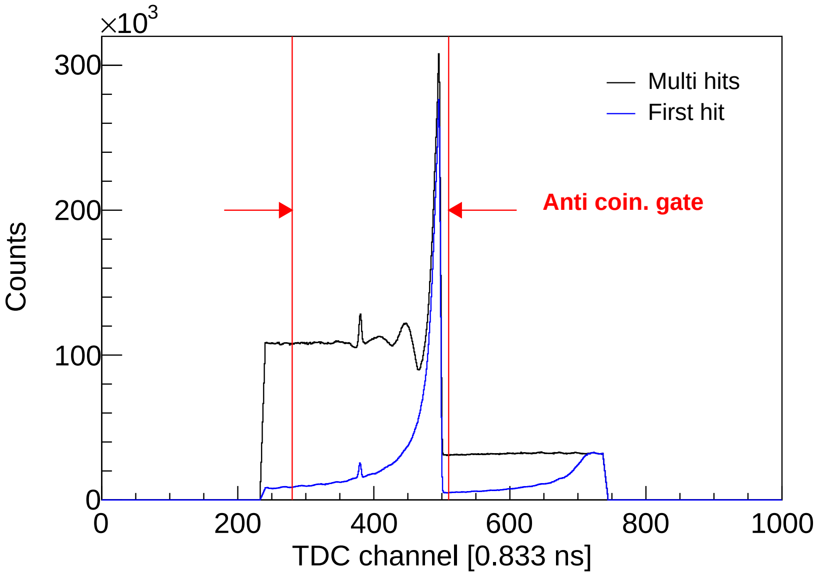

Figure 3.15: Typical timing distribution of the BGO counters. The black line shows a timing distribution for all the hits in the multi-hit TDCs, while the blue line shows a timing distribution for the first hit in each event.

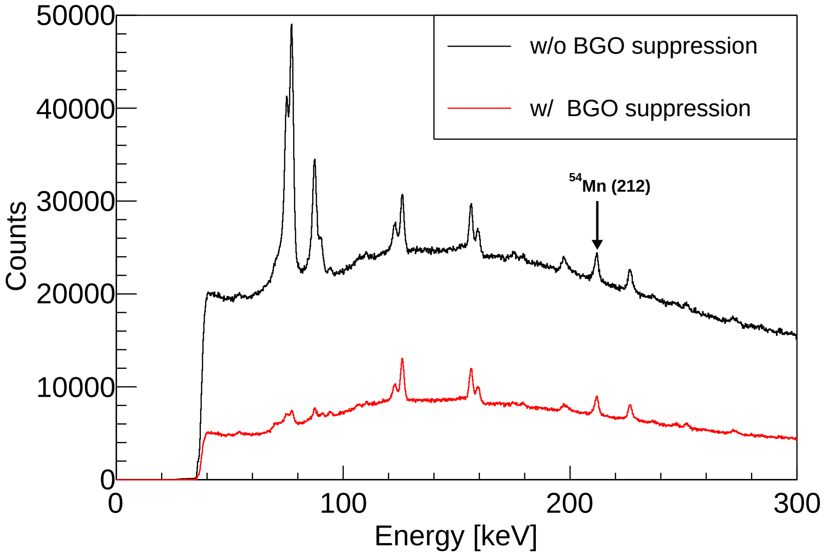

Figure 3.16: Energy spectrum of Ge detectors for the $(K^{-}, p)$ reaction w/ and w/o BGO suppression.

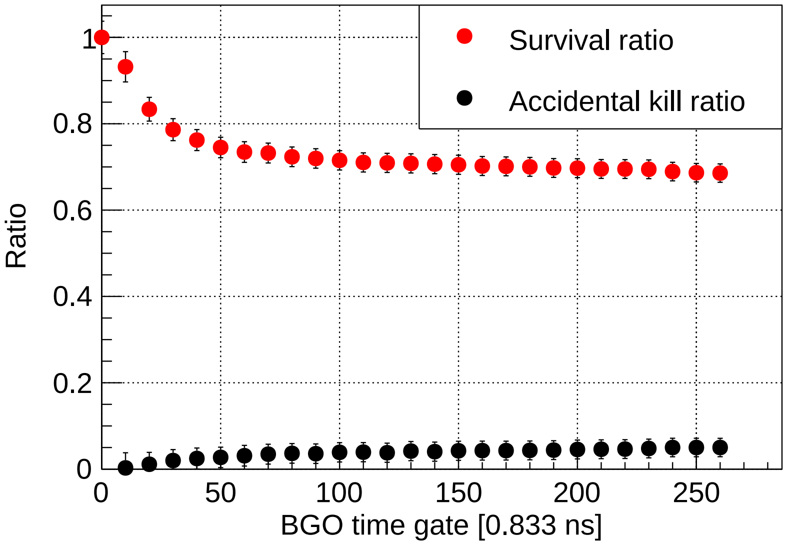

Figure 3.17: The dependence of BGO time-gate width on peak survival ratio and the accidental kill ratio for the $\gamma$ ray from $^{54}$Mn.

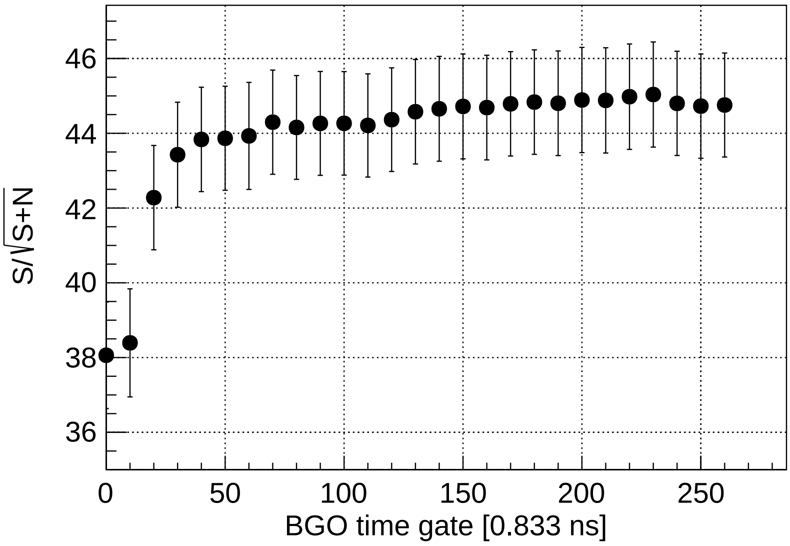

Figure 3.18: Dependence of the BGO time-gate width on peak significance ($S/\sqrt{S+N}$) for the $\gamma$ ray from $^{54}$Mn.

### 3.3.2 Energy calibration of Ge detectors

In the present analysis, we focused on the energy region of 100-400 keV. Thus, only two $\gamma$-ray peaks from $^{176}$Lu, at 202.843 and 306.791 keV were used for the energy calibration of the Ge detectors. The calibration data was taken using the LSO×Ge trigger described in Sec. 2.6.2. It is known from previous studies that the measured energy shifts to the lower side by less than 1 keV under the beam-on condition. Therefore, the calibration was done using data obtained in beam-on period. Even in the beam-on condition, clear peaks were obtained with the LSO×Ge trigger. Figure 3.19 shows the energy distribution for the LSO×Ge trigger data in the beam on and off periods. The energy calibration was performed run-by-run (every hour) to correct for gain drift of Ge detector due to change of crystal complifier temperature. The positions of the LSO counters and the prescale factor for the LSO×Ge trigger were optimized so that the one-hour $\gamma$-ray yield from $^{176}$Lu was over 300 counts for each Ge crystal.

The accuracy of the energy calibration was evaluated using $\gamma$ rays from $^{133}$Ba and $^{152}$Eu sources. The data was taken under the on-beam condition for several hours. Six reference $\gamma$-ray peaks in the range of 100-400 keV were used for the evaluation. Figure 3.20 shows the residuals between the measured energy and the known energy by using data summed up for all of the Ge crystals. The accuracy was estimated to be less than 0.2 and 0.1 keV in the range of 100-200 and 200-400 keV, respectively.

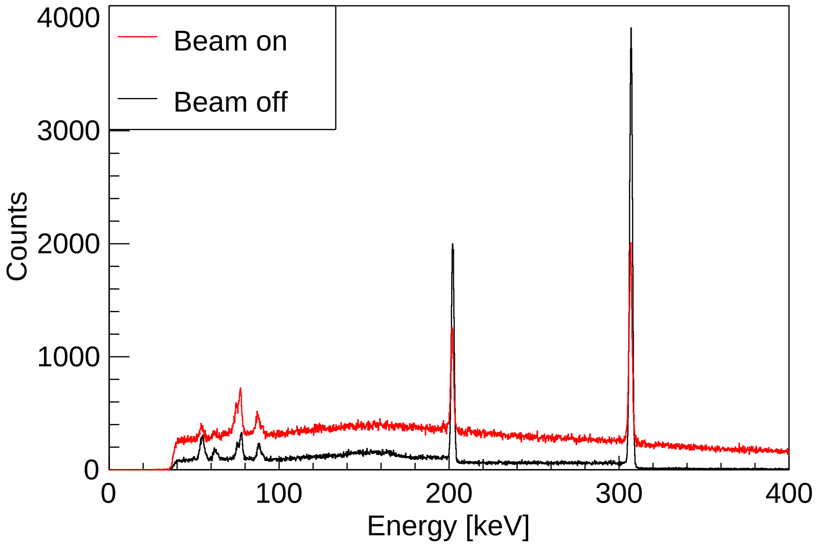

Figure 3.19: Energy distribution for the LSO×Ge trigger data in the beam on/off periods.

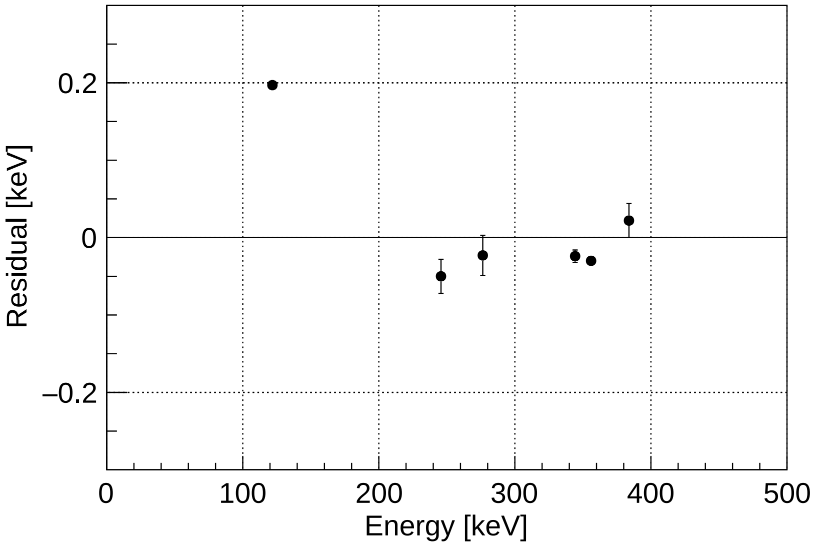

Figure 3.20: Residuals between measured $\gamma$-ray energy and known energy for all Ge detectors.

### 3.3.3 Performance of Hyperball-X’

#### Energy resolution

The energy resolution of the Ge detectors was evaluated by the $\gamma$ rays from $^{152}$Eu in the on-beam and off-beam condition. Figure 3.21 shows energy dependence on the energy resolution ($\sigma$). The energy resolutions in the region of interest (100-400 keV) were 0.85, 0.92 and 0.94 keV for the $\gamma$ ray of 121, 245 and 344 keV, respectively.

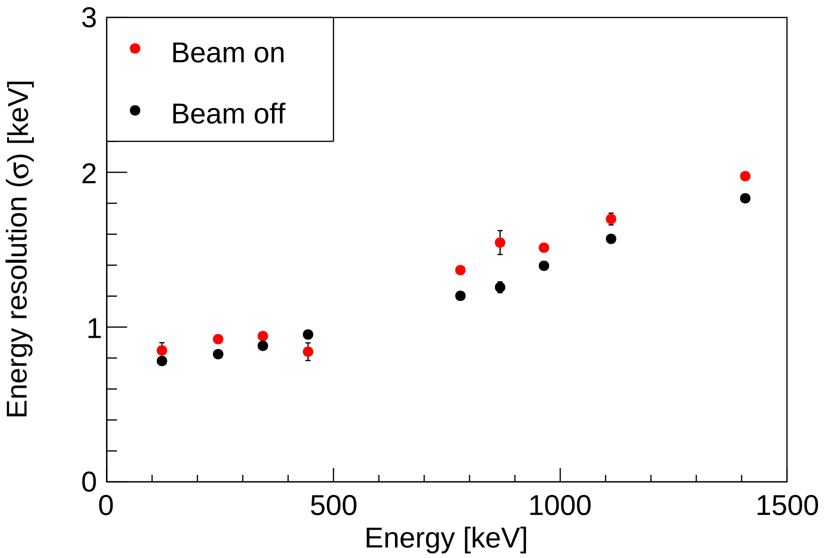

Figure 3.21: Energy dependence of the energy resolution of Ge detectors, which was evaluated with the $\gamma$ rays from $^{152}$Eu in the on-beam and off-beam condition.

## Detection efficiency

### Photopeak efficiency

The photopeak efficiency was measured with checking sources at the target position under the off-beam condition. Figure 3.22 shows the energy dependence on the photopeak efficiency for the entire Ge detectors. The efficiency was measured by $^{133}$Ba and $^{152}$Eu sources. On the other hand, the absolute efficiency was measured by a $^{60}$Co source and an NaI counter. The black line in Fig. 3.22 is the efficiency curve without the iron target estimated by a Monte-Carlo simulation using the GEANT4 code. The red line represents the efficiency curve with the target. The efficiency curve without the target was scaled to fit measured data with a scaling factor of 0.67. The scaling factor smaller than 1 would be attributed to uncertainty on shape and size of the Ge crystals in the simulation. The photopeak efficiency for $\Xi^-$Fe atomic X rays of 172 and 286 keV were obtained to be 2.9% and 2.5%, respectively, from the efficiency curve with the target. The systematic error by scaling the simulation curve was estimated to be 9%. The uncertainties of the source intensity was 1.8% and 1.9% for $^{133}$Ba and $^{152}$Eu sources, respectively.

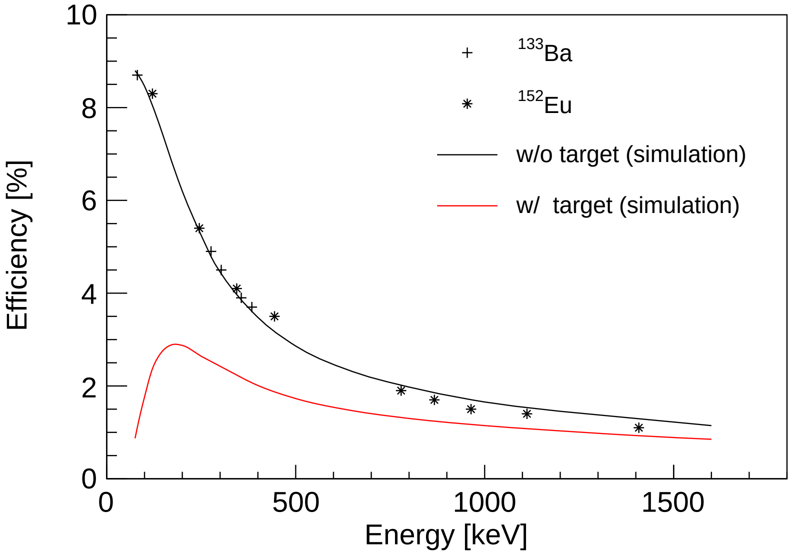

Figure 3.22: Energy dependence on the photopeak efficiency for entire Ge detectors.

**Live time**

There are two reasons for a reduced live time of the Ge detectors in the on-beam condition. One is signal pileup caused by mulitple hits within the integration time of the ORTEC 671 shaping amplifier. The other is baseline distortion of the shaping amplifier after the preamplifier reset as described in 3.3.1. Typical dead times due to these reasons were around 10 $\mu$s per hit and 50-600 $\mu$s per reset, respectively. The live time reduction is significant under the conditions with high intensity and high energy beams. In general, the live time can be estimated using the dead time, the counting rate and the reset rate. However, since the beam has bunch structure, the effective live time is lower than that with simple estimation. Therefore, the effective live time under such a beam condition was estimated using peak counts of the $\gamma$ ray from a $^{60}$Co source. Data taking was performed under three conditions: clock trigger without beam (1), clock trigger with beam (2) and KK trigger with beam (3). The live time is defined as

$$\text{Live time} = \frac{\text{Counts of } \gamma \text{ ray for which the energy inforamtion was read correctly}}{\text{Counts of } \gamma \text{ rays photoelectrically absorbed by Ge crystals}} \quad (3.8)$$

Figure 3.23 shows the ADC distribution obtained under the trigger conditions (1), (2) and (3). The live time under each trigger condition was evaluated using a 1333 keV $\gamma$-ray peak. The live time under the condition (1) is regarded as 100% because the counting rate and reset rate was low enough. Thus, the live times in the condition (2) and (3) were obtained by comparing the peak counts of the $\gamma$ ray under each condition with that of the condition (1) as reference. The live time of the condition (2) was 75.2%, corresponding to the beam structure not considered. The live time of the condition (3), with the beam structure taken into account, was 61.1%, which is regarded as an effective live time for the $\Xi^-$ atomic X ray measurement as well.

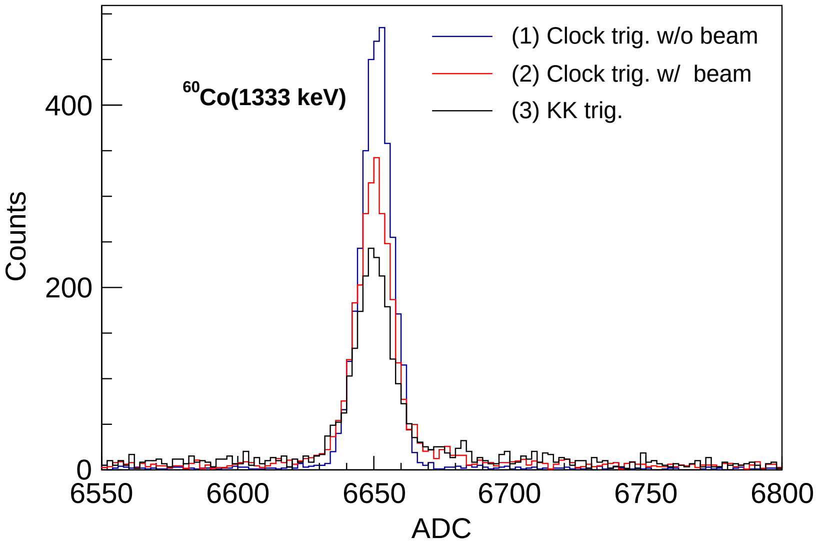

Figure 3.23: 1333 keV $\gamma$-ray peak from $^{60}$Co source obtained under the trigger condition (1), (2) and (3).

### Summary of the performance of Hyperball-X'

Table 3.1 summarize the performance of Hyperball-X' for the energy region of interest.

Table 3.1: Summary of the performance of Hyperball-X'.

| | |
|---|---|
| Calibration accuracy | 0.2 keV for 100-200 keV<br>0.1 keV for 200-400 keV |
| Energy resolution ($\sigma$) | 0.85 keV for 121 keV<br>0.94 keV for 344 keV |
| Photopeak efficiency | 2.9% for 172 keV<br>2.5% for 286 keV |
| Live time for KK trigger data | 61% |
| Peak survival ratio after BGO sup. | 70% |

The total efficiency of Hyperball-X' is obtained by the product of the photopeak efficiency, the live time and the peak survival ratio after the BGO suppression. The total efficiency was 1.2% and 1.1% for the $\Xi^-$Fe atomic X rays of 172 keV and 286 keV, respectively.

## 3.4 Selecting $\Xi^-$ with high stopping probability

In the analysis described in Sec. 3.2, it is possible to identify the $\Xi^-$ production by calculating missing mass. However, most of produced $\Xi^-$s did not stop in the target because of $\Xi^-$ decaying in-flight and $\Xi^-$ going out of the target. When a $\Xi^-$ does not stop in the target, it eventually decays and gives false hits to the Ge detectors. The $\Xi^-$ decays into $\Lambda$ with $\pi^-$ emission with a 99% branching ratio. When the $\Lambda$ decays to $p\pi^-$, produced $\pi$ mesons hit surrounding materials and make background $\gamma$ rays. On the other hand, the $\Lambda$ decay to $n\pi^0$ followed by $\pi^0$ decay to $2\gamma$ also make background. For these reasons, the decay of $\Xi^-$ produces background in the X-ray spectrum. Therefore, a good signal to noise ratio could be obtained by determining whether the $\Xi^-$ has stopped in the target using information on the missing momentum and the reaction vertex. However, the missing momentum had uncertainty due to Fermi motion of a proton. The reaction point also had uncertainty due to a worse z-vertex resolution. In this analysis, the events with high stopping probability of $\Xi^-$ were selected based on a simulation using GEANT4 code. Prior to this simulation, a missing mass (MM) selection described in Sec. 4.1 (MM<1.44 GeV/$c^2$) was applied in order to focus on the $p(K^-, K^+)\Xi^-$ process. The $\Xi^-$ momentum is given as

$$\vec{p}_{\Xi^-} = \vec{p}_{K^-} + \vec{p}_p - \vec{p}_{K^+} \tag{3.9}$$

where $\vec{p}_p$ is Fermi motion momentum of a proton in the target nucleus, and $\vec{p}_{K^-}$ and $\vec{p}_{K^+}$ are the measured momenta of the beam and the scattered particles, respectively. The missing momentum ($\vec{p}_{K^-} - \vec{p}_{K^+}$) is expected to have a correlation with the stopping probability of $\Xi^-$. Figure 3.24 shows the missing momentum distribution and the correlation between the missing momentum and the scattering angle with the polyethylene target. Figure 3.25 shows the same distributions for the iron target. The missing momentum was corrected by considering the momentum loss of the beam $K^-$ and the scattered $K^+$ in the target and the spectrometer counters. This correction was confirmed by comparing the missing momentum obtained from the data with the polyethylene target and that from a kinematic calculation for the elementary $\Xi^-$ production as shown in Fig. 3.24

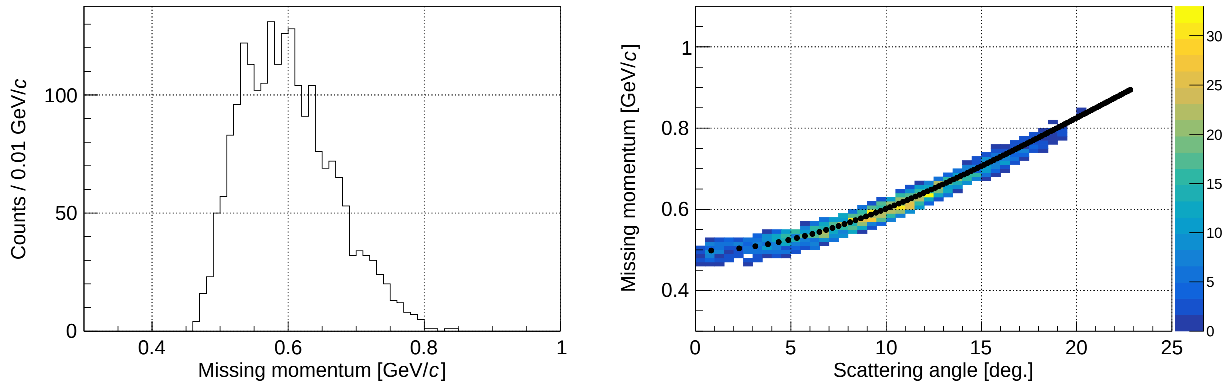

Figure 3.24: Missing momentum distribution and the correlation between the missing momentum and the scattering angle with the polyethylene target. A missing mass selection ($1.30 < \mathrm{MM} < 1.34$ GeV/$c^2$) was applied to select the elementary $\Xi^-$ production events (see Fig. 3.10). Black dots in the right figure show calculated values for $p(K^-, K^+)\Xi^-$ reaction with $P_{K^-} = -1.8$ GeV/$c$.

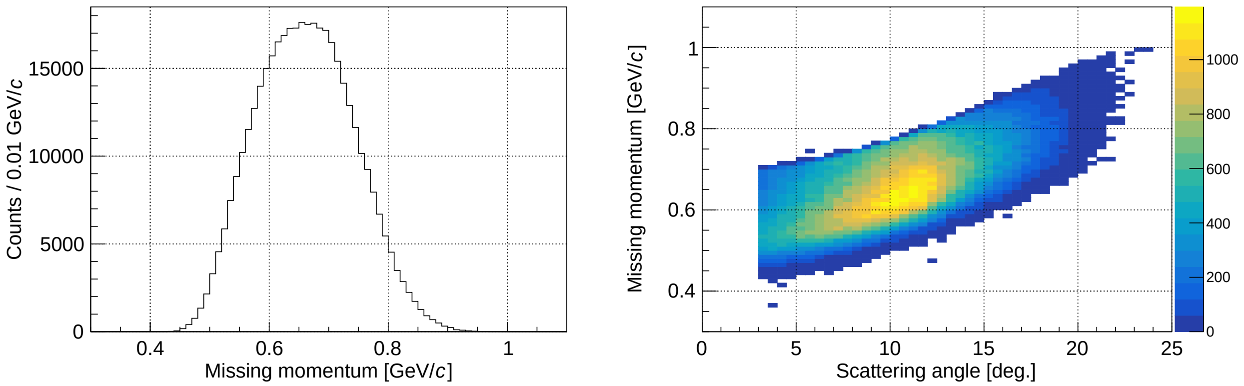

Figure 3.25: Missing momentum distribution and the correlation between the missing momentum and the scattering angle with the iron target. A missing mass selection (MM $< 1.44$ GeV/$c^2$) was applied as described in Sec. 4.1.

In the simulation, the $\Xi^-$ particles were generated 100 times for each analyzed event by randomly changing Fermi motion momentum vectors and reaction vertex points. The momentum distribution of the proton in $^{56}$Fe nucleus was assumed as the same as that obtained from $^{58}$Ni$(e, e'p)$ data [32]. Figure 3.26 shows the momentum distribution from $^{58}$Ni$(e, e'p)$ for $7 \leqq E \leqq 9.5$ MeV ($E$: separation energy). This momentum distribution corresponds to that of protons at the outermost shell ($1f$ state). We assumed that the beam $K^-$s reacted only with the protons at the outermost shell in $^{56}$Fe nucleus and only the distribution in Fig. 3.26 was used.

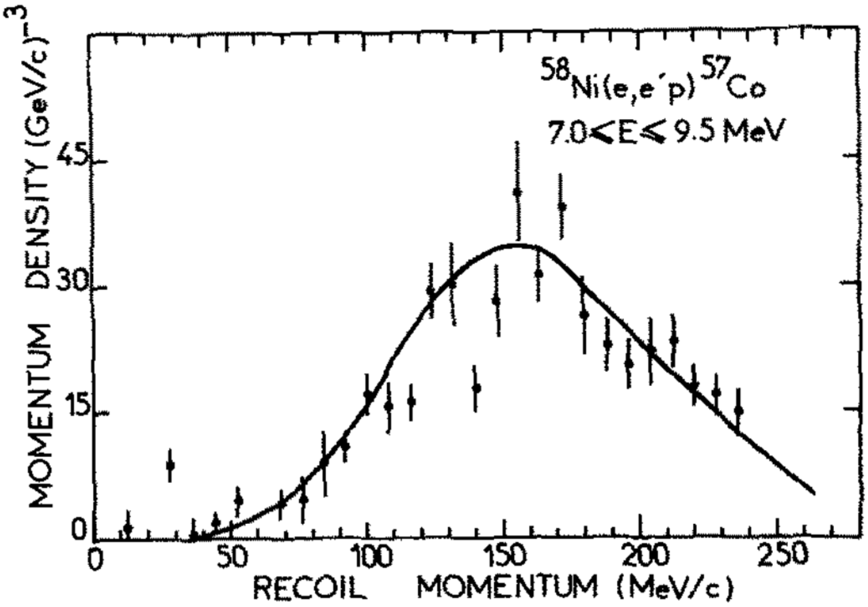

Figure 3.26: Momentum distribution from $^{58}$Ni$(e,e'p)$ for $7 \leqq E \leqq 9.5$ MeV ($E$: separation energy) [32]. The solid line represents a calculation (DWIA calculation).

Figure 3.27 shows the stopping probability of $\Xi^-$ obtained from the simulation. Figure 3.28 shows the correlation between the stopping probability of $\Xi^-$ and the missing momentum ($\vec{p}_{K^-} - \vec{p}_{K^+}$). The average of the stopping probability of $\Xi^-$ was obtained to be 9.2% for MM<1.44 GeV/$c^2$. If the distribution of the Fermi momentum in Fig. 3.26 shifts by 10 MeV/c, the average changes by 0.2%. To select events with a high stopping probability of $\Xi^-$, the threshold for the stopping probability was set. The threshold value was determined to maximize a signal to noise ratio ($S/\sqrt{N}$) for X rays of $\Xi^-$Fe atom (172 and 286 keV). $S$ is expected X-ray yield given as

$$S = N_{stopped\ \Xi^-} \times \epsilon_{HBX} \times P_{\Xi^-(n,l)} \tag{3.10}$$

where $N_{stopped\ \Xi^-}$ is the expected value of number of stopped $\Xi^-$s at a certain threshold obtained from Fig. 3.27, $\epsilon_{HBX}$ is the total efficiency of Hyperball-X', and $P_{\Xi^-(n,l)}$ is a ratio of the number of $\Xi^-$s reaching the $(n,l)$ state to the yield of $\Xi^-$ atom. $P_{\Xi^-(n,l)}$ values predicted by theoretical calculation is 0.3 and 0.1 for $P_{\Xi^-(7I)}$ and $P_{\Xi^-(6H)}$, respectively. $N$ is number of background obtained by integrating $\pm 5\sigma$ range of 172 and 286 keV in the spectrum when a certain threshold is applied. Figure 3.29 shows the expected X-ray yield of $\Xi^-$Fe atom ($S$), the number of background ($N$) and a signal to noise ratio ($S/\sqrt{N}$) with a certain threshold for stopping probability. The best signal to noise ratio was obtained with the threshold of 10%.

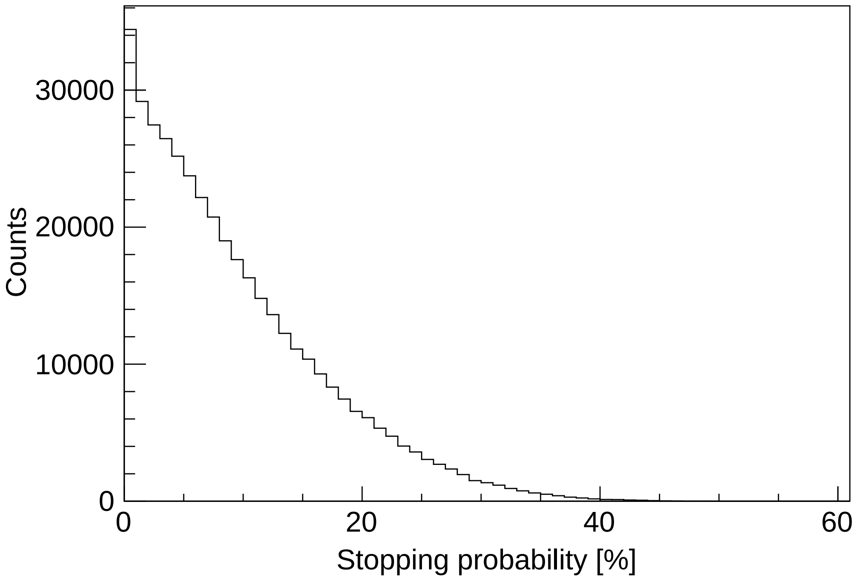

Figure 3.27: Stopping probability of $\Xi^-$ particles obtained from the simulation.

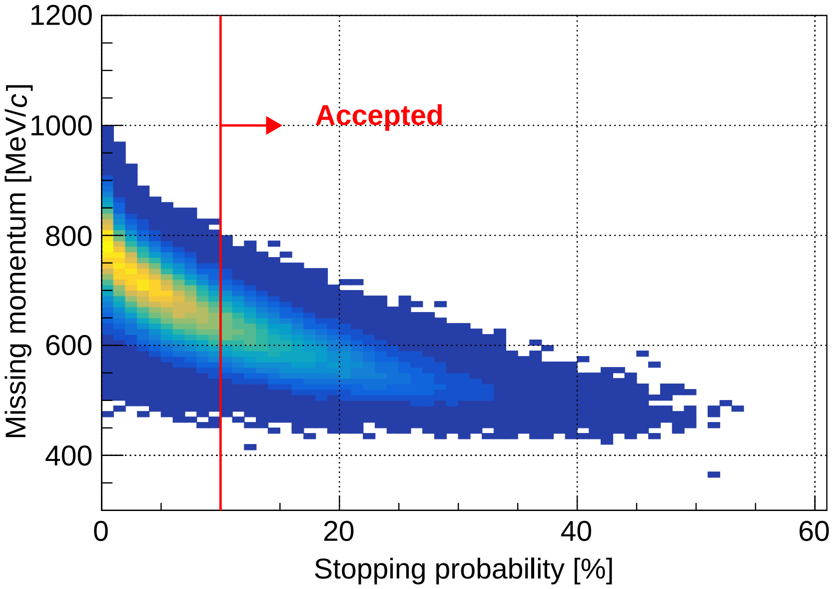

Figure 3.28: Correlation between the stopping probability of $\Xi^-$ and missing momentum ($\vec{p}_{K^-} - \vec{p}_{K^+}$).

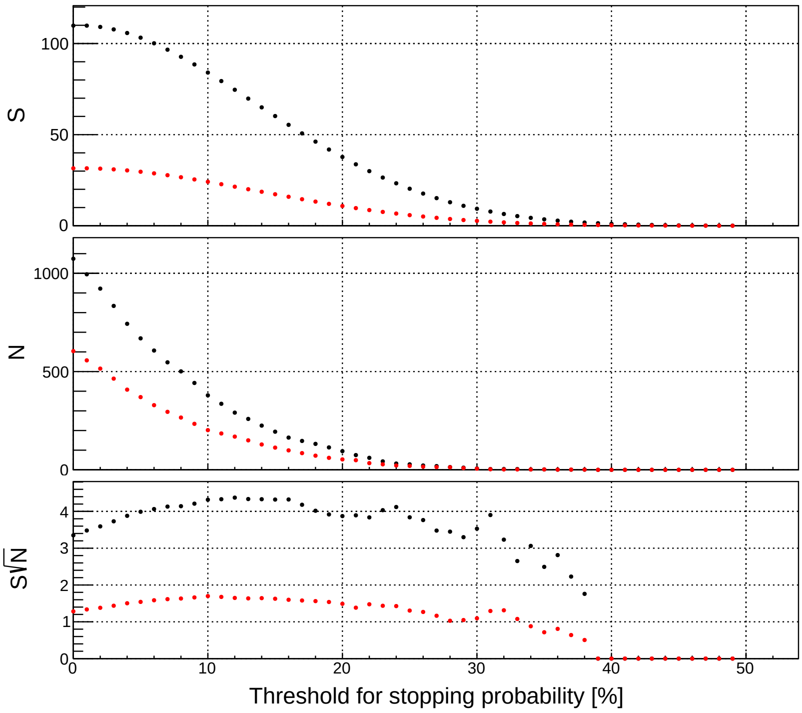

Figure 3.29: Expected X-ray yield of $\Xi^-$Fe atom ($S$), number of background ($N$) and a signal to noise ratio ($S/\sqrt{N}$) with a certain threshold for the stopping probability.

# Chapter 4

# Result and discussion

## 4.1 Missing mass selection

The missing mass distribution contains components of not only $\Xi^-$ production but also $\Xi^-(1530)$ and $\Xi\pi$ production. Furthermore, the background events due to misidentification of scattered particles also contaminate it. In this section, missing mass selection considering these factors is described.

To select $\Xi^-$ production events, the missing mass distribution was estimated by a Monte-Carlo simulation. In this simulation, four processes of the $(K^-, K^+)$ reaction were considered,

a. $K^-p \to K^+\Xi^-$,

b. $K^-p \to K^+\Xi^-(1530)$,

c. $K^-p \to K^+\Xi^0\pi^-$, and

d. $K^-p \to K^+\Xi^-\pi^0$.

All processes were simulated as two-body and three-body decays following uniform phase space. The momentum distribution of the protons in Fe nucleus is the same as in the simulation for the $\Xi^-$ stopping probability described in Sec. 3.4. The cross section of each process used in this simulation was based on the experimental data. The total cross sections of the processes a, b, c, and d were 175±16, 28±6, 16±4, and 34±4 $\mu$b, respectively at 1.7 GeV/$c$ beam $K^-$ momentum [33]. Furthermore, the momentum and the angular acceptance of the KURAMA spectrometer were considered. Figure 4.1 shows a simulated missing mass distribution for each processes of the $(K^-, K^+)$ reaction.

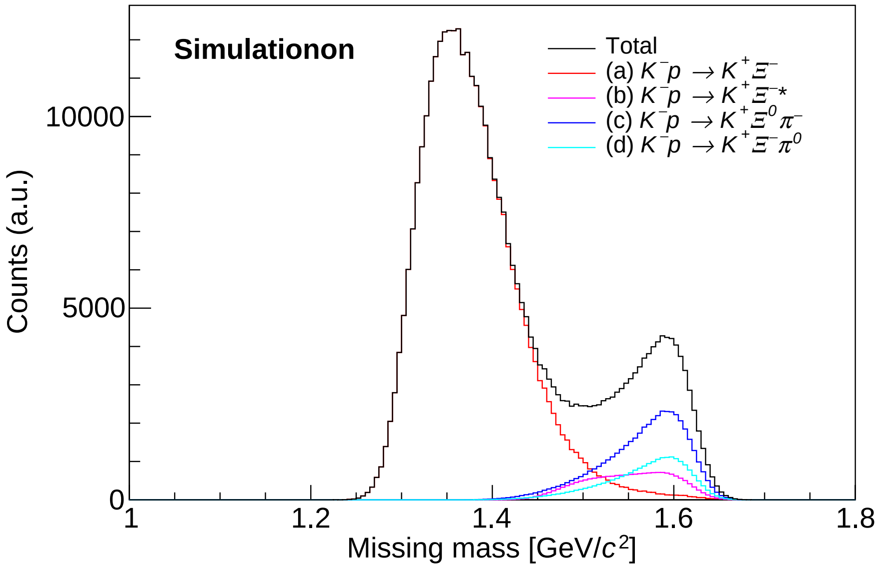

Figure 4.1: Simulated missing mass distribution for each process of the $(K^-, K^+)$ reaction.

In the masss selection of the scattered particle (see Fig 4.2), the background ratio within the mass square gate, the $\pm 2\sigma$ region from the mean of $K^+$ peak, was estimated by fitting the mass square distribution with a Gaussian function and a constant background. The background ratio was estimated for each 0.1 GeV/$c$ step of the scattered particle momentum ($p_{scat}$) in the range of 0.5-1.3 GeV/$c$ because the mass square gate was adjusted for each momentum region taking account of mass square resolution. Figure 4.2 shows the fitting result in a representative case of 1.2-1.3 GeV/$c$. Table 4.1 summarizes the $K^+$ yield and background ratio within the mass square gate for each momentum region.

Table 4.1: $K^+$ yield and background ratio within the mass square gate for each momentum region.

| Momentum region [GeV/$c$] | $K^+$ yield [$10^4$] | BG ratio[%] |
|---|---|---|
| 0.5-0.6 | 2.0 | 11 |
| 0.6-0.7 | 3.0 | 13 |
| 0.7-0.8 | 2.6 | 19 |
| 0.8-0.9 | 2.0 | 26 |
| 0.9-1.0 | 2.6 | 26 |
| 1.0-1.1 | 8.6 | 15 |
| 1.1-1.2 | 11.9 | 15 |
| 1.2-1.3 | 8.9 | 17 |

The background structure in the missing mass distribution was estimated by selecting regions at the left and right sides of the mass square gate, correspoing to the red shaded regions in Fig 4.2. Figure 4.3 shows the missing mass distribution for $1.2 < p_{scat} < 1.3$ GeV/$c$ region. The blue and red lines show the background structures when the left and the right sides of the mass square gate were selected, respectively. The number of background events was scaled as shown in table 4.1. The ratio of number of the left background to the right background was assumed to be 1:1. Then, magenta line shows the distribution of the total background which will be used for optimizing the missing mass selection described below.

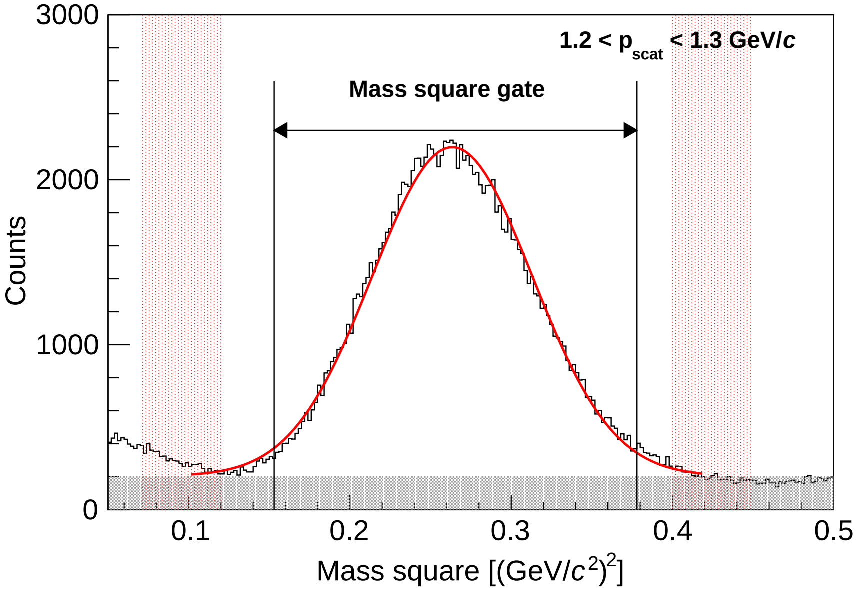

Figure 4.2: Estimation of background ratio in the mass square distribution of the scattered particle using a Gaussian function and a constant background function.

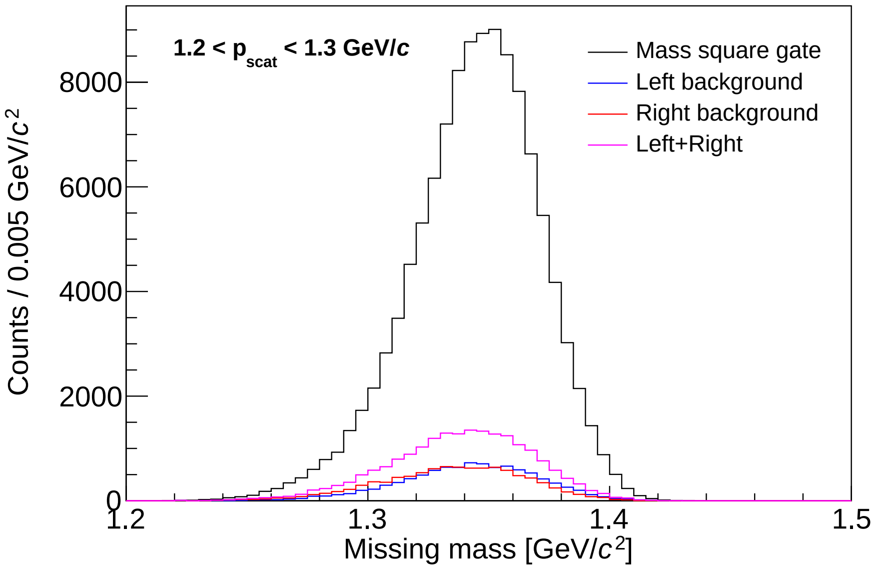

Figure 4.3: Missing mass distribution for the $1.2 < p_{scat} < 1.3$ GeV/$c$ region. A magenta line shows the total background due to misidentification of scattered particles.

Figure 4.4 shows comparison of the missing mass distributions of the experimental data and the simulation. A black shaded distribution shows the background estimated from the mass square distribution. The distribution of each $(K^-, K^+)$ reaction process was scaled to fit the experimental data of the subtracted background. A red line shows the estimated missing mass distribution of the combined distribution of each $(K^-, K^+)$ reaction process and the background. A upper end of the missing mass gate was set to 1.44 GeV/$c^2$, where a signal to noise ratio $(S/\sqrt{S+N})$ in maximum. $S$ is the number of events in the simulated distribution of the process (a). $N$ was taken from the number of events in the distribution subtracting the distribution (a) from the experimental data because the estimated distribution did not well reproduce the experimental data. The $\Xi^-$ yield from the process (a) in the missing mass gate was $3.5 \times 10^5$. We considered the error of $\Xi^-$ yield caused by a scaling factor for the simulated distribution (a) by a chi-square fitting. The error of $\Xi^-$ yield was estimated to be $\pm 2\%$.

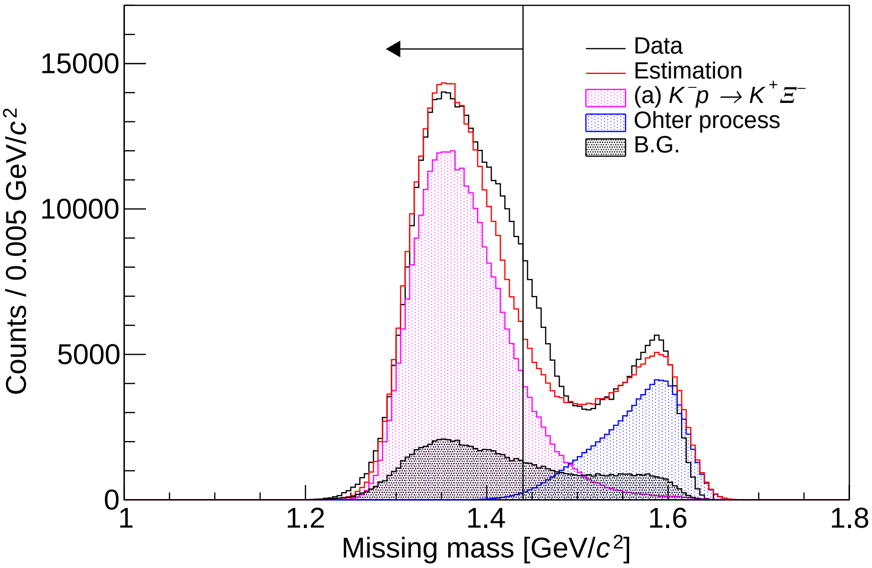

Figure 4.4: Comparison of the missing mass distributions of experimental data and simulation.

## 4.2 X-ray spectra

Figure 4.5 shows the X-ray spectra in the energy region of 0-400 keV obtained by analysis of the magnetic spectrometers and Hyperball-X' without and with the BGO suppression. For these spectra, the missing mass selection was applied to the $\Xi^-$ production region as described in Sec. 4.1. The background continuum and the X-ray peaks from Bi (77 and 87 keV) were greatly suppressed with 70% survival ratio for other peaks as described in Sec. 3.3.1. So, hereafter, we only show X-ray spectra with the BGO suppression applied with the optimal time gate of 230 ns. Figure 4.6(a) shows a spectrum with only the missing mass selection (the same as the red spectrum in Fig. 4.5). Figure 4.6(b) shows a spectrum by selecting $\Xi^-$ particles with a high stopping probability of more than 10% as described in Sec. 3.4 in addition to the missing mass selection.

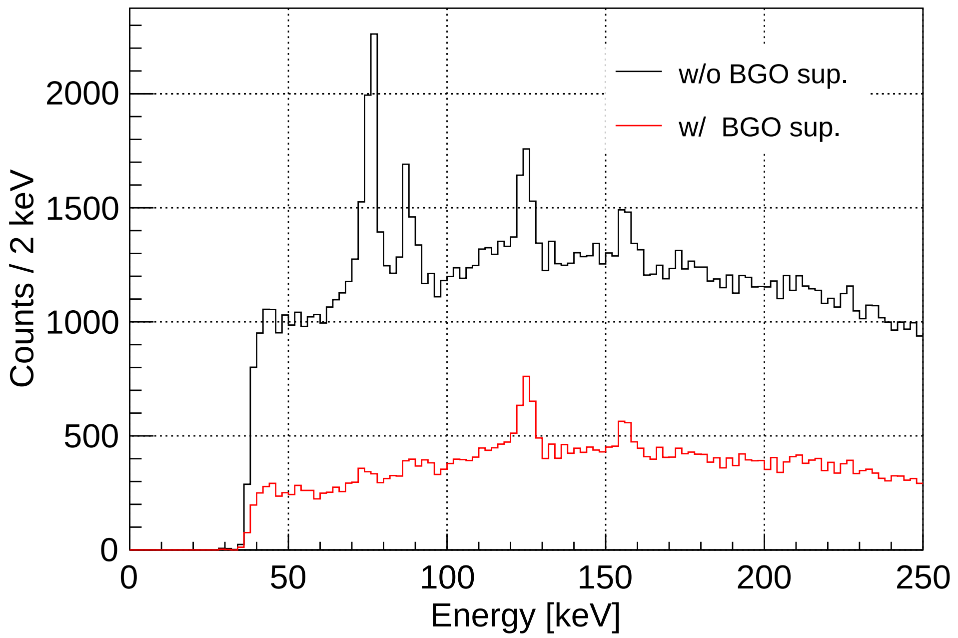

Figure 4.5: X-ray spectra measured by Hyperball-X' in coincidence with the $(K^-, K^+)$ reaction without and with BGO suppression. In the spectrum without the BGO suppression, peaks from Bi X rays are observed at 77 and 87 keV, but are greatly suppressed in the spectrum with the BGO suppression.

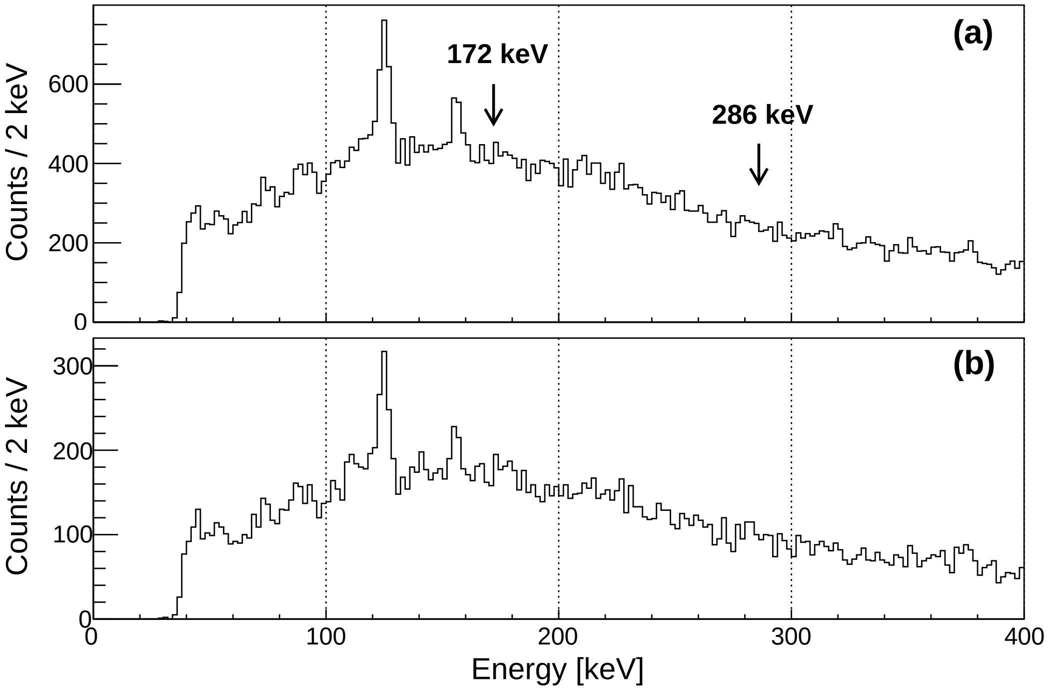

Figure 4.6: X-ray spectra measured by Hyperball-X' in coincidence with the $(K^-, K^+)$ reaction. For spectrum (a), missing mass selection was applied to the $\Xi^-$ production region. For spectrum (b), the events with a high stopping probability of $\Xi^-$ particles were selected.

Peak search was carried out for the spectra (a) and (b) by evaluating a peak significance defined as

$$\text{Peak significance} = \frac{S}{\sqrt{S+N}}, \tag{4.1}$$

where $S$ is the peak counts obtained by fitting with a Gaussian function and a liner background function, $N$ is the value obtained by integrating the linear background function over a range of $\pm 3\sigma$ around the mean position of the peak. The width of the Gaussian function was fixed at 0.9 keV, corresponding to the measured energy resolution. The fitting was performed by shifting the peak position by a fixed step of 1 keV in the range of 70–400 keV. The fitting range was ±10 keV around the peak position for each fitting. Figure 4.7 and 4.8 show the results of the peak search in the X-ray spectrum (a) and (b), respectively. In both spectra, three peaks at 126, 156, 378 keV were found with the peak significance of more than $3\sigma$. These $\gamma$ rays were from manganese nuclei ($^{55}$Mn, $^{54}$Mn and $^{53}$Mn) produced by reactions between the iron target and the beam particles. On the other hand, no clear peaks with significance of more than $3\sigma$ were observed around 172 and 286 keV corresponding to the expected energies of the $\Xi^-$ Fe atomic X rays.

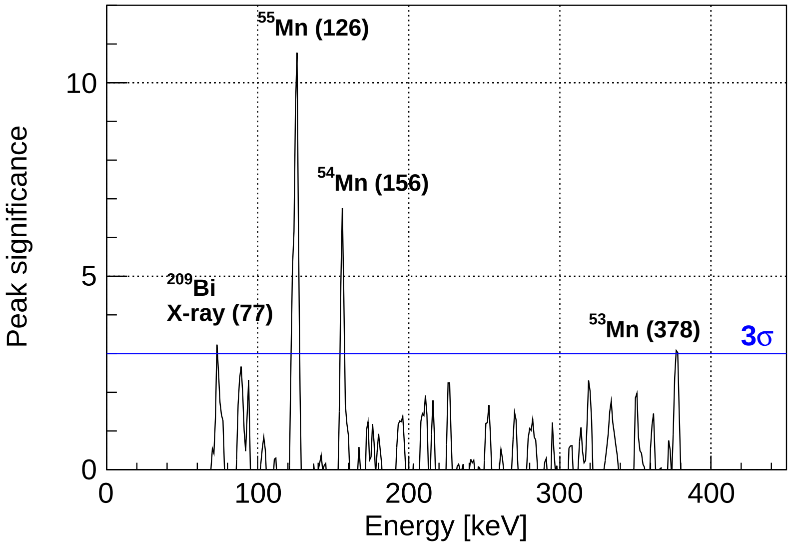

Figure 4.7: A result of the peak search in the X-ray spectrum (a).

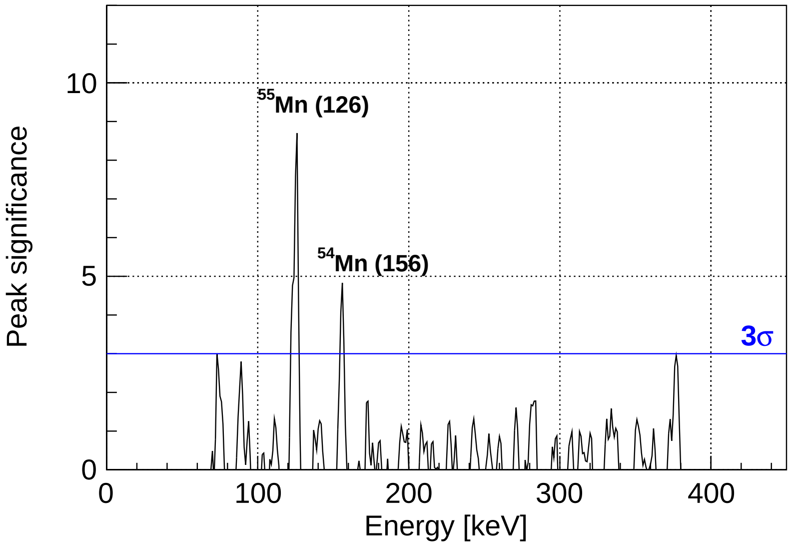

Figure 4.8: A result of the peak search in the X-ray spectrum (b).

## 4.3 Intensity of the $\Xi^-$Fe atomic X ray

Since no clear peak was observed, the upper limit of the X-ray intensity per stopped $\Xi^-$ was evaluated for the X-ray spectrum (b). The intensity, $R_X$, is given as

$$R_X^{(n,l\ \rightarrow\ n-1,l-1)} = BR_{E1}^{(n,l\ \rightarrow\ n-1,l-1)} \times P_{\Xi^-(n,l)}, \tag{4.2}$$

where $BR_{E1}^{(n,l\,\rightarrow\,n-1,l-1)}$ is a branching ratio of E1 transition, and $P_{\Xi^-(n,l)}$ is a ratio of the number of $\Xi^-$s reaching the $(n,l)$ state to the yield of the $\Xi^-$ atom. In the circular orbit states without effect of strong interaction, the branching ratio is 1. $R_X$ is also given from the measured values as

$$R_X = \frac{N_X}{N_{stopped\ \Xi^-} \times \epsilon_{HBX}}, \tag{4.3}$$

where $N_X$ is the X-ray yield obtained by the peak fitting, $N_{stopped\ \Xi^-}$ is the number of $\Xi^-$s stopped in the target corresponding to the yield of $\Xi^-$ atom, and $\epsilon_{HBX}$ is the total efficiency of Hyperball-X' as described in Sec. 3.3.3. The expected number of $\Xi^-$ stopped in the target was estimated based on a simulation as shown in Fig. 3.27. The expected $N_{stopped\ \Xi^-}$ values were 29661 and 22705 for all the events (a) and the events above the threshold of 10% stopping probability (b), respectively.

Figure 4.9 shows the X-ray spectrum (a) around 172 keV and the upper limit of $R_X^{(7I\rightarrow 6H)}$ with 90% confidence level (CL). Considering a possibility of the X-ray energy shift, the upper limit of $R_X^{(7I\rightarrow 6H)}$ in the range of 172±10 keV is obtained to be 0.22 for the X-ray spectrum (a). Figure 4.10 shows the X-ray spectrum (b) around 172 keV and the upper limit when $\Xi^-$s with the high stopping probability (>10%) were selected. In this case, the 90%-CL upper limit of $R_X^{(7I\rightarrow 6H)}$ in the range of 172±10 keV is obtained to be 0.19. For the 286 keV X ray, Fig. 4.11 shows the X-ray spectrum (a) and the upper limit of $R_X^{(6H\rightarrow 5G)}$. The 90%-CL upper limit of $R_X^{(6H\rightarrow 5G)}$ in the range of 286±10 keV is obtained to be 0.20 for the X-ray spectrum (a). Figure 4.12 shows that for the X-ray spectrum (b) and the 90%-CL upper limit of $R_X^{(6H\rightarrow 5G)}$ for the 286 keV X ray, and the upper limit in the range of 286±10 keV is obtained to be 0.21.

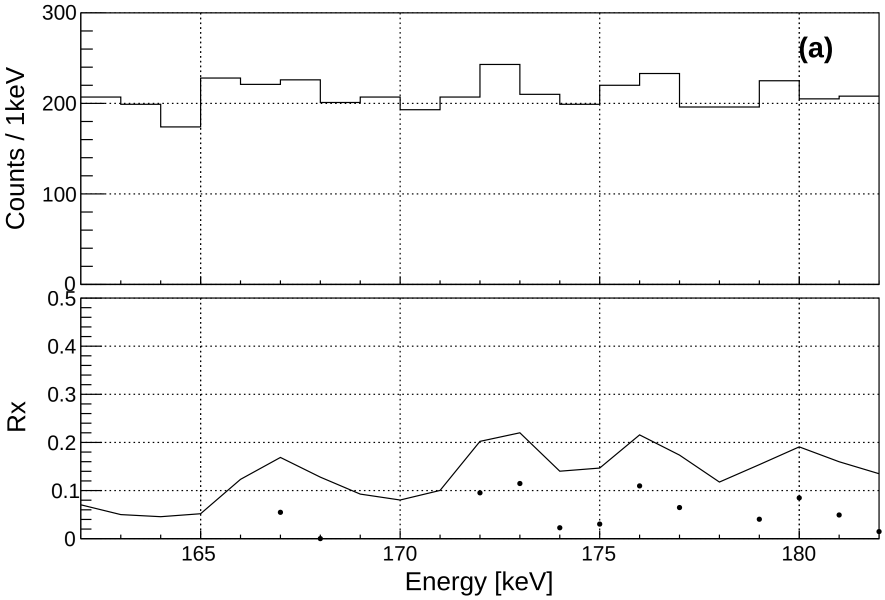

Figure 4.9: X-ray spectrum (a) around 172 keV and the upper limit of $R_X^{(7I\to 6H)}$. In the bottom figure, the dots show the fitted mean values and the line shows the 90%-CL upper limit.

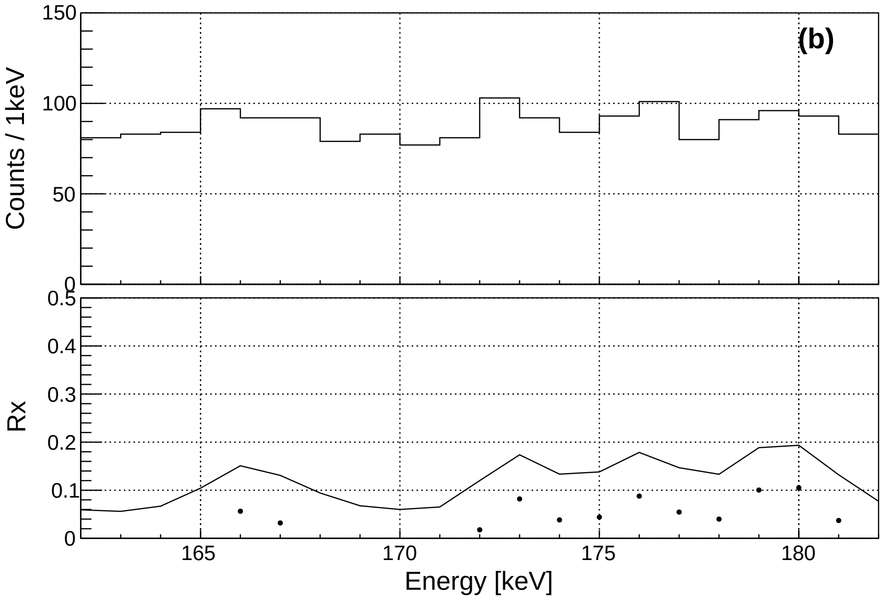

Figure 4.10: X-ray spectrum (b) and the upper limit of $R_X^{(7I\to 6H)}$ in the case where $\Xi^-$s with the high stopping probability (>10%) were selected. In the bottom figure, the dots show the fitted mean values and the line shows the 90%-CL upper limit.

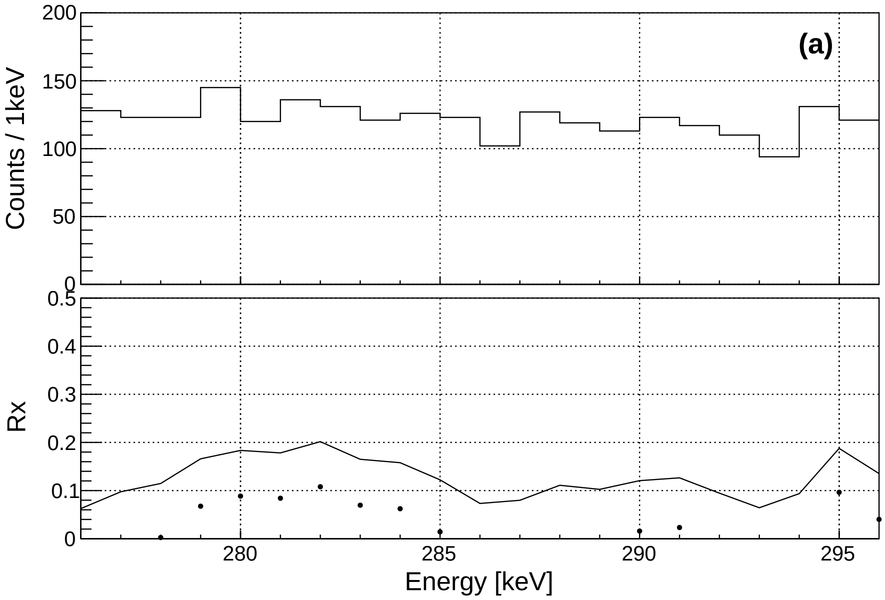

Figure 4.11: X-ray spectrum (a) around 286 keV and the upper limit of $R_X^{(6H\to5G)}$. In the bottom figure, the dots show the fitted mean values and the line shows the 90%-CL upper limit.

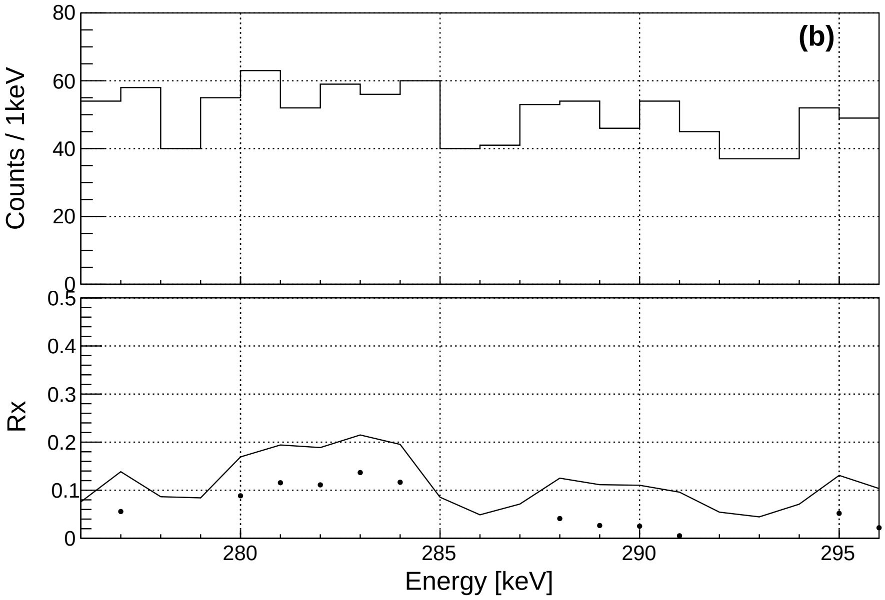

Figure 4.12: X-ray spectrum (b) and the upper limit of $R_X^{(6H\to5G)}$ when $\Xi^-$s with the high stopping probability (>10%) were selected. In the bottom figure, the dots show the fitted mean values and the line shows the 90%-CL upper limit.

## 4.4 Discussion

In this analysis, the upper limit of $R_X^{(7I\to 6H)}$ in the range of 172±10 keV is obtained to be 0.19 in the 90% confidence level from the X-ray spectrum for $\Xi^-$s with a high stopping probability as shown in Fig. 4.10. We considered ambiguity in the $N_{stopped\ \Xi^-}$ caused by a finite probability that the produced $\Xi^-$ exits from the target nucleus, which is called emission probability. The emission probability of the produced $\Xi^-$ hyperon, $R_{emit}$, in the $(K^-, K^+)$ reaction was measured in past experiments. Table 4.2 summarizes the emission probability of $\Xi^-$ hyperon for nuclear emulsion, $^{12}$C and $^{9}$Be targets in the KEK-E176, KEK-E224 and BNL-E906 experiments. In the BNL-E906 experiment, the rates of direct-escape and quasi-elastic reaction ($R_{escape}$ and $R_{scat}$) were obtained as follows. Here, the direct-escape and quasi-elastic reaction are the cases where the produced $\Xi^-$ does not react with other nucleons in the target nucleus and where it is elastically scattered with other nucleons, respectively.

Table 4.2: A summary of the emission probability of $\Xi^-$, $R_{emit}$, in the $(K^-, K^+)$ reaction.

| Experiment | Target | $R_{emit}$ [%] | $P_{K^-}$ [GeV/$c$] |
|---|---|---|---|
| KEK-E176 [34] | Nuclear emulsion | $73.9^{+4.5}_{-4.6}$ | 1.66 |
| KEK-E224 [35] | $^{12}$C in $CH_2$ | 80.1±2.4 | 1.66 |
| BNL-E906 [36] [37] | $^{9}$Be | 78.1±10.1 | 1.8 |

$$R_{escape} = 63.6 \pm 8.2\% \tag{4.4}$$

$$R_{scat} = 14.5 \pm 2.6\% \tag{4.5}$$

The BNL-E906 Collaboration considered that the rest of about 20% of produced $\Xi^-$s may undergo inelastic interaction such as $\Xi^- p \to \Lambda\Lambda(\Sigma)$ or $\Xi^- p \to \Xi^0 n$ in the target nucleus where the $(K^-, K^+)$ reaction occurred. For the nuclear emulsion target (KEK-E176), the target was regarded as a mixture of H, light (C, N, O) and heavy (Br, Ag) nuclei with a ratio of 15 : 38 : 47, which is calculated by the product of the element composition of the emulsion and a mass number dependence $A^{0.37}$ of the cross section. Since the proton number of iron nucleus (Z=26) is just between those of the heavy nuclei (Z=35,47) and those of the H and light nuclei (Z=1, 12,14,16), and the reaction rates on the heavy nuclei and the H and light nuclei are about half and half, we presume that the $R_{emit}$ with the iron target is comparable to that with the emulsion target ($R_{emit} = 73.9^{+4.5}_{-4.6}$). Assuming that $R_{emit}$ is 70% with the iron target, the 90%-CL upper limit of $R_X^{(7I\to 6H)}$ in the range of 172±10 keV is 0.27.

In the theoretical calculation [24], $P_{\Xi^-(7I)}$ is expected to be 0.3 with $\alpha = -0.056$ in Eq. 1.2. This $\alpha$ value was based on experimental data of $\Sigma^-$ atomic X ray and a cascade calculation [38] although the value may have ambiguity due to differences in hyperon mass and target nuclei. $R_X^{(7I\to 6H)}$ is thus estimated to be 0.3 with $BR_{E1}^{(7I\to 6H)}$ $\sim 1$ because a negligibly small effect of strong interaction is expected for the $7I$ state. The obtained upper limit of $R_X$ from the present experiment is lower than the predicted value or comparable to that taking $R_{emit}$ into account. Figure 4.13 shows the calculated absolute yields (yields per $\Sigma^-$ or $\Xi^-$ stop) of X-ray transitions in $\Sigma^-$ and $\Xi^-$ Pb atoms as a function of the initial population parameter $\alpha$ in the cascade calculation [38]. We hope that the present upper limit will be followed by such cascade calculations to constrain the $\alpha$ value for $\Xi^-$ Fe atom.

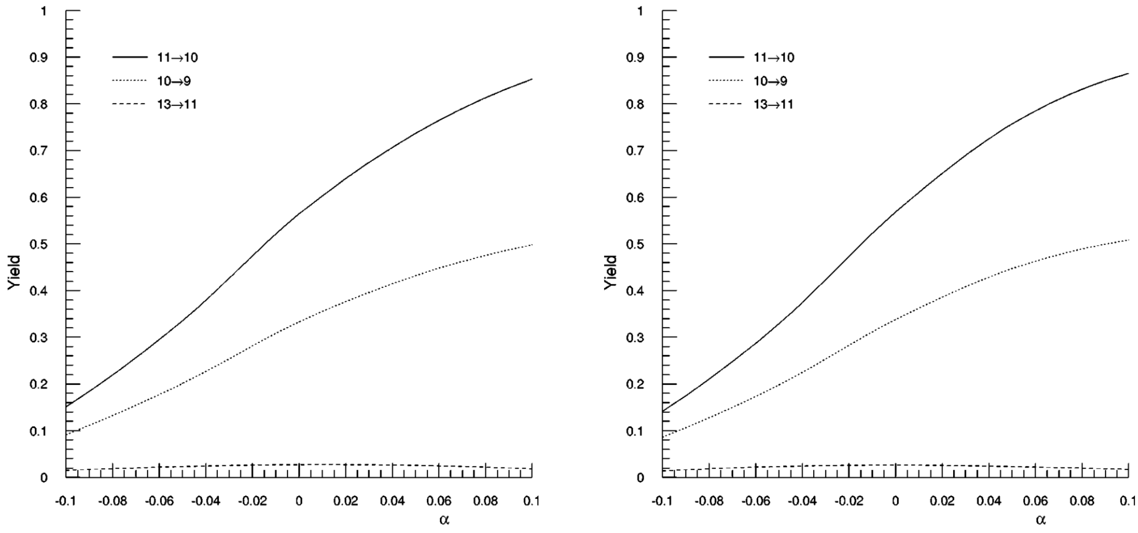

Figure 4.13: Calculated absolute yields of X-ray transitions in $\Sigma^-$ and $\Xi^-$ Pb atoms as a function of the initial population parameter $\alpha$. The left figure shows for $\Sigma^-$ Pb atoms and the right figure shows for $\Xi^-$ Pb atoms. Results are shown for $n_i \to n_f$ transitions with $l = n - 1$ [38].

In the present study, no clear peak with a significance $(S/\sqrt{S+N})$ greater than 3 was observed in the X-ray spectrum. For observation of X-ray peak with the $R_X^{(7I\to 6H)}$ of less than 0.2, more statistics and/or improvement of signal-to-noise ratio are necessary. In this analysis, the peak count at 172 keV was obtained to be $S = 35 \pm 29$ from the X-ray spectrum (a) with the number of background events in the range of $172{\pm}2\sigma$ $(\sigma = 0.9)$ keV region of $N = 745$. We estimated how much statistics would be required for the peak significance greater than 3 with the same $S/N$ ratio as the present result. Taking the obtained mean value of $S$, 6 times statistics is required. To realize higher statistics, we can reconsider the acceptance of Ge detectors and the beam intensity. Considering an extension form the present experimental setup, the total acceptance can be increased up to a factor of $\sim 2$ by adding detectors upstream and downstream of the target while interferences with the trigger counters should be considered. Furthermore, a higher intensity beam should be used for higher statistics. J-PARC was designed to be operated with about four times higher primary beam intensity than the current level. However, in such a high intensity beam condition, the live time of Ge detector will decrease significantly and limit statistics. Therefore, the development to improve the live time, such as introducing a waveform digitizing method for the read out of the Ge detectors, is necessary. The $\Xi^-$Fe atomic X ray of $(7I \rightarrow 6H)$ transition would be observed with these improvements. Furthermore, for future measurements, we should think about adding detectors near or in the target to enhance $\Xi^-$ stop events, leading to better signal-to-noise ratio in the X-ray spectrum.

# Chapter 5

# Summary

The J-PARC E03 experiment was performed in 2020-2021 to obtain information on the $\Xi^-$-nuclear interaction via $\Xi^-$ atomic X-ray spectroscopy with an iron target. To produce $\Xi^-$ particles via the $(K^-, K^+)$ reaction, a $K^-$ beam with the momentum of 1.8 GeV/$c$ was irradiated to the iron target. Some of the $\Xi^-$ particles were stopped in the target and then captured by iron atoms, resulting in the formation of $\Xi^-$ Fe atoms. Beam $K^-$ particles and scattered $K^+$ particles were particle identified and momentum analyzed by the beam line spectrometer and the KURAMA spectrometer, respectively, for the identification of the $p(K^-, K^+)\Xi^-$ reaction. In addition, the germanium detector array, Hyperball-X' was used to detect X rays from the $\Xi^-$ Fe atoms.

Most of the produced $\Xi^-$ particles decay before stopping in the target and made background events. Then, the analysis was performed to remove the background by selecting the events with a high stopping probability of $\Xi^-$ particle using a Monte-Carlo simulation. Nevertheless, no clear peak with more than $3\sigma$ significance was observed from the obtained X-ray spectrum. The 90%-CL upper limit of the X-ray intensity per stopped $\Xi^-$ for $(7I \rightarrow 6H)$ transition $(R_X^{(7I\rightarrow 6H)})$ was estimated considering the expected number of stopped $\Xi^-$s. The upper limit of 0.19 was obtained by selecting the $\Xi^-$ with a high stopping probability. Assuming that the emission probability of the produced $\Xi^-$ is 70% with the iron target, the upper limit is 0.27. The obtained upper limit from the present experiment is lower than the predicted value ($R_X^{(7I\rightarrow 6H)} = 0.3$), or comparable to that considering the emission probability.

# Acknowledgment

First, I would like to thank all the people who provided advice and supported for the accomplishment of the present thesis. In particular, I am grateful to Prof. Hirokazu Tamara for his advice and support for my research from the time I was assigned to the laboratory. In addition, I would like to express my gratitude to Prof. Mifuyu Ukai from KEK and Dr. Takeshi Yamamoto from JAEA for their advice on the analysis and writing the preset thesis. I am grateful to Prof. Kiyoshi Tanida and Dr. Manami Fujita from JAEA for advising me on the analysis. I would like to all the collaborators of the J-PARC E03 experiment. Finally, I would like to thank my family for their encouragement.

# Bibliography

[1] K. Miwa et al., Phys. Rev. C **104**, 045204 (2021).

[2] O. Hashimoto and H. Tamura, Prog. Part. Nucl. Phys. **57**, 564 (2006).

[3] G. Backenstoss, T. Bunaciu, J. Egger, H. Koch, A. Schwitter, and L. Tauscher, Z. Physik A **273**, 137 (1975).

[4] C. J. Batty et al., Phys. Lett. B **74**, 27 (1978).

[5] R. J. Powers et al., Phys. Rev. C **47**, 1263 (1993).

[6] J. Schaffner-Bielich, Nucl. phys. A **804**, 309 (2008).

[7] M. M. Nagels et al., Phys. Rev. C **99**, 044003 (2019).

[8] K. Sasaki et al., Nucl. Phys. A **998**, 121737 (2020).

[9] M. Kohno, Phys. Rev. C **100**, 024313 (2019).

[10] T. Iijima et al,. Nucl. Phys. A **546**, 588 (1992).

[11] P. Khaustov et al., Phys. Rev. C **61**, 054603 (2000).

[12] T. Nagae et al., AIP Conf. Proc. **2130**, 1, 020015 (2019).

[13] S. Aoki et al., Prog. Theor. Phys. **89**, 493 (1993).

[14] S. Aoki et al., Phys. Lett. B **355**, 45 (1995).

[15] A. Ichikawa et al., Phys. Lett. B **500**, 37 (2001).

[16] K. Nakazawa et al., Prog. Theor. Exp. Phys. **2015**, 3, 033D02 (2015).

[17] E. Hiyama and K. Nakazawa, Annu. Rev. Nucl. Part. Sci. **68**, 13159 (2018).

[18] S.H. Hayakawa et al., Phys. Rev. Lett. **126**, 6, 062501 (2021).

[19] M. Yoshimoto et al., Prog. Theor. Exp. Phys. **2021**, 7, 073D02 (2021).

[20] E. Friedman, A. Gal, Phys. Lett. B **837**, 137640 (2023).

[21] S. Acharya et al., Phys. Rev. Lett. **123**, 112002 (2019).

[22] M. Fujita et al., Prog. Theor. Exp. Phys. **2022**, 12, 123D01 (2022)

[23] M. Fujita, Doctoral thesis, Tohoku University (2019).

[24] T. Koike, private communication (2020).

[25] A. T. M. Aerts and C. B. Dover, Phys. Rev. C **28**, 450 (1983).

[26] R. Honda et al., Nucl. Inst. and Meth. A **787**, 157 (2015).

[27] Hadron Universal Logic Module – Open-It, https://openit.kek.jp/project/HUL/HUL.

[28] M. Fujita et al., Nucl. Inst. and Meth. A **1042**, 167439 (2022).

[29] Y. Igarashi et al., IEEE Trans. Nucl. Sci. **57**, 618 (2020).

[30] J. Myrheim and L. Bugge, Nucl., Inst. Meth. **160**, 43 (1979).

[31] Electromagnetics Suite 15.0, Maxwell 3D, ANSYS, Inc., Canonsburg, PA, USA.

[32] J. Mougey et al., Nucl. Phys. A **262**, 461 (1976).

[33] P.M. Dauber et al., Phys. Rev. **179**, 1262 (1969).

[34] S. Aoki et al., Phys. Rev. A **644**, 365 (1998).

[35] K. Nakazawa, Nucl. Phys. A **639**, 345 (1998).

[36] T. Tamagawa et al., Nucl. Phys. A **691**, 234 (2001).

[37] T. Tamagawa, Doctoral thesis, Tokyo University (2000).

[38] C. J. Batty, E. Friedman, and A. Gal, Phys. Rev. C **59**, 295 (1999).